2010

New Panoramic View of ^{12}CO and 1.1 mm Continuum Emission in the Orion A Giant Molecular Cloud. I. Survey Overview and Possible External Triggers of Star Formation

Y Shimajiri

R Kawabe

S Takakuwa

M Saito

T Tsukagoshi

See next page for additional authors

Recommended Citation

Shimajiri, Y; Kawabe, R; Takakuwa, S; Saito, M; Tsukagoshi, T; Momose, M; Ikeda, N; Akiyama, E; Austermann, JE; Ezawa, H; Fukue, K; Hiramatsu, M; Hughes, D; Kitamura, Y; Kohno, K; Kurono, Y; Scott, KS; Wilson, GW; Yoshida, A; and Yun, Min, "New Panoramic View of ^{12}CO and 1.1 mm Continuum Emission in the Orion A Giant Molecular Cloud. I. Survey Overview and Possible External Triggers of Star Formation" (2010). *PUBLICATIONS OF THE ASTRONOMICAL SOCIETY OF JAPAN*. 1128.
10.1093/pasj/63.1.105

New Panoramic View of ^{12}CO and 1.1 mm Continuum Emission in the Orion A Molecular Cloud. I. Survey Overview and Possible External Triggers of Star Formation

Yoshito Shimajiri[1,2], Ryohei Kawabe[2,3], Shigehisa Takakuwa[4], Masao Saito[3,5], Takashi Tsukagoshi[6], Munetake Momose[7], Norio Ikeda[8], E. Akiyama [7], Austermann, J. E. [9,10] H. Ezawa[3], K. Fukue[1,5], M. Hiramatsu[4], D. Hughes[11], Y. Kitamura[8], K. Kohno[6], Y. Kurono[3,5], Scott, K. S.[12], G. Wilson[9], A. Yoshida[13], M.S. Yun[9],

*

[1] *Department of Astronomy, School of Science, University of Tokyo, Bunkyo, Tokyo 113-0033, Japan*

[2] *Nobeyama Radio Observatory, Minamimaki, Minamisaku, Nagano 384-1805, Japan*

[3] *National Astronomical Observatory of Japan, Osawa 2-21-1, Mitaka, Tokyo 181-8588, Japan*

[4] *Academia Sinica Institute of Astronomy and Astrophysics, P.O. Box 23-141, Taipei 10617, Taiwan*

[5] *ALMA Project Office, National Astronomical Observatory of Japan, Osawa 2-21-1, Mitaka, Tokyo 181-8588, Japan*

[6] *Institute of Astronomy, Faculty of Science, University of Tokyo, Osawa 2-21-1, Mitaka, Tokyo, 181-0015, Japan*

[7] *Institute of Astrophysics and Planetary Sciences, Ibaraki University, Bunkyo 2-1-1, Mito 310-8512, Japan*

[8] *Institute of Space and Astronoutical Science, Japan Aero space Exploration Agency, Yoshinodai 3-1-1, Sagamihara, Kanagawa 229-8510, Japan*

[9] *Department of Astronomy, University of Massachusetts, Amherst, MA 01003, USA*

[10] *Center for Astrophysics and Space Astronomy, University of Colorado, Boulder, CO 80309, USA*

[11] *Instituto Nacional de Astrofísica, Óptica y Electrónica (INAOE), Aptdo. Postal 51 y 216, 72000 Puebla, México*

[12] *Department of Physics and Astronomy, University of Pennsylvania, Philadelphia, PA 19104, USA*

[13] *Department of Earth and Planetary Sciences Tokyo Institute of Technology, 2-12-1, Ookayama, Meguro-ku, Tokyo 152-8551, Japan*

yoshito.shimajiri@nao.ac.jp

(Received ; accepted)

Abstract

We present new, wide and deep images in the 1.1 mm continuum and the ^{12}CO (J=1–0) emission toward the northern part of the Orion A Giant Molecular Cloud

(Orion-A GMC). The 1.1 mm data were taken with the AzTEC camera mounted on the Atacama Submillimeter Telescope Experiment (ASTE) 10 m telescope in Chile, and the ^{12}CO (J=1–0) data were with the 25 beam receiver (BEARS) on the NRO 45 m telescope in the On-The-Fly (OTF) mode. The present AzTEC observations are the widest ($1.^{\circ}7 \times 2.^{\circ}3$, corresponding to 12 pc $\times$ 17 pc) and the highest-sensitivity ($\sim$9 mJy beam^{-1}) 1.1 mm dust-continuum imaging of the Orion-A GMC with an effective spatial resolution of $\sim 40''$. The ^{12}CO (J=1–0) image was taken over the northern $1.^{\circ}2 \times 1.^{\circ}2$ (corresponding 9 pc $\times$ 9 pc) area with a sensitivity of 0.93 K in $T_{\rm MB}$, a velocity resolution of 1.0 km s^{-1}, and an effective spatial resolution of $21''$. With these data, together with the MSX 8 μm, Spitzer 24 μm and the 2MASS data, we have investigated the detailed structure and kinematics of molecular gas associated with the Orion-A GMC and have found evidence for interactions between molecular clouds and the external forces that may trigger star formation. Two types of possible triggers were revealed; 1) Collision of the diffuse gas on the cloud surface, particularly at the eastern side of the OMC-2/3 region, and 2) Irradiation of UV on the pre-existing filaments and dense molecular cloud cores. Our wide-field and high-sensitivity imaging have provided the first comprehensive view of the potential sites of triggered star formation in the Orion-A GMC.

Key words: stars:formation — ISM: molecules — ISM: cloud

1. Introduction

Giant Molecular Clouds (GMCs) are main sites of star formation. There are approximately three thousand GMCs in our Galaxy, with a size of 10 - 80 pc and a mass of 10^4 - 5 $\times$ 10^6 $M_{\odot}$ (Solomon et al. 1977). While only low-mass stars form in dark clouds (Myers et al. 1995; Momose et al. 1998; Saito et al. 1999; Takakuwa et al. 2004), in GMCs both low-mass and high-mass stars form (Megeath 1994; Homeier & Alves 2005; Yonekura et al. 2005). There are many uncertain aspects of star formation in GMCs, such as the core mass function (CMF), its link to the initial mass function (IMF), massive star formation, and cluster formation. Hence, studies of star formation in GMCs are imperative to the comprehensive understanding of star formation.

Theoretical studies of massive star formation and cluster formation have proposed that external effects on molecular clouds, such as ultraviolet (UV) radiation from HII regions, supernova remnants (SNRs), molecular outflows, and cloud-cloud collisions are required to trigger the massive-star (Elmegreen 1998) and cluster formation (Whitworth et al. 1994; Hosokawa & Inutsuka 2005; Nakamura & Li 2007). Furthermore, it is proposed that the shape of the

* Last update: Sep, 20, 2010

CMF could also be affected by the presence of those external effects (Zinnecker & Yorke 2007). Hence, it is essential to unveil the global picture of those external effects on molecular gas in GMCs. It is, however, not yet clear how ubiquitous those external effects and the triggered star formation in GMCs are. Unbiased and extensive mapping observations of GMCs in molecular and dust continuum emission, covering an entire GMC and resolving individual cores with a typical size of ~ 0.1 pc, and the comparison with the images at other wavelengths, are required to approach the global picture of star formation in GMCs.

The Orion-A GMC, with an extent of $\sim 10^{\circ}$ (corresponding to ~ 72 pc) in the southern part of Orion constellation, is the nearest (d= 400 pc; Menten et al. 2007; Sandstrom et al. 2007; Hirota et al. 2008) GMC and one of the well studied regions in star formation studies (Tatematsu et al. 1993; Lis et al. 1998; Tatematsu et al. 1998; Johnstone & Bally 1999; Aso et al. 2000; Stanke et al. 2002; Tsujimoto et al. 2002; Takahashi et al. 2008; Takahashi et al. 2009; Davis et al. 2009). Many authors have proposed that the Orion-A GMC is externally affected, both at small (~ 0.1 pc) and large scales ($\sim$ several $\times$ 10 pc), by molecular outflow, ionizing radiation, SNRs, and stellar winds generated by the Orion OB association, from its morphological structure, velocity structure, and the stellar ages (Cowie et al. 1979; Bally et al. 1987; Sandell & Knee 2001; Yokogawa et al. 2003; Wilson et al. 2005; Lee & Chen 2009). OB stars embedded in the Orion-A GMC form the HII region, M 42, 43, and NGC 1977 (Goudis et al. 1982). Molecular outflows driven from OMC-2/FIR 3 and FIR 6c interact with the surrounding dense cores, which triggers gravitational instabilities in the dense cores and the next generation star formation (Shimajiri et al. 2008; Shimajiri et al. 2009). These facts imply that the Orion-A GMC is one of the most suitable GMCs for an unbiased extensive study of triggered star formation.

With the advent of multi-beam receivers at millimeter wavelengths, wide-field mapping observations over several square degrees at an angular resolution of several $\times$ 10″ are now feasible. In this paper, we present a wide, sensitive 1.1-mm dust-continuum and ^{12}CO (J=1–0) line imaging of the northern part of the Orion A GMC with the AzTEC camera mounted on the ASTE telescope and BEARS mounted on the Nobeyama (NRO) 45-m telescope, respectively. The aim of this paper is to reveal the overall structure of the Orion-A GMC from a cloud ($\geq$ 10 pc) to a core scale (≤ 0.1 pc) with the wide coverage and high sensitivity, and specifically, to unveil the global picture of the external triggers of star formation in the GMC from the comparison with the near-infrared (NIR) and mid-infrared (MIR) images. The detailed physical processes of individual triggered star formation will be discussed in the forthcoming papers. The 1.1 mm dust-continuum emission is optically thin and traces the total mass of molecular gas in cores and envelopes (Enoch et al. 2006). The ^{12}CO (J=1–0) emission traces low-density gas ($\leq 10^3$ cm^{-3}) and is usually optically thick and easily thermalized. Hence, the ^{12}CO emission traces global structures of GMCs, and the peak intensities of the ^{12}CO emission at the emission ridge often reflect kinetic temperature of molecular gas.

This paper is organized as follows: in section 2, the NRO 45-m and AzTEC/ASTE observations are described. In section 3, we present results of the AzTEC 1.1 mm continuum and the NRO ^{12}CO (J=1–0) mapping of the Orion-A GMC. In section 4, we focus on the possible external triggers of the star formation in the Orion-A GMC. First, we describe the possibility that the entire Orion-A GMC is influenced over $\sim$ several $\times$ 10 pc scale by the external effect. Then, we show the region irradiated by the UV radiation from OB stars embedded in the Orion-A GMC over a few pc-scale. In section 5, we summarize this paper.

2. Observations

2.1. AzTEC/ASTE Observations

From October to December 2008, we carried out 1.1 mm dust-continuum observations toward the $1.^{\circ}7 \times 2.^{\circ}3$ region in the northern part of the Orion A molecular cloud with the AzTEC camera (Wilson et al. 2008) equipped in the ASTE 10 m telescope (Ezawa et al. 2004; Kohno et al. 2004) located at Pampa la Bola (altitude = 4800 m), Chile. The weather conditions during our observing period were moderate and the typical opacity at 225 GHz was in the range of 0.1 - 0.2. The AzTEC camera mounted on the ASTE telescope is an 144-element bolometric camera tuned to operate in the 1.1 mm atmospheric window, and provides an angular resolution of 28″ in full width at half maximum (FWHM)(Wilson et al. 2008). Observations were performed in the raster scan mode toward a pair of $100' \times 100'$ fields, centered on $(\alpha_{J2000},\delta_{J2000})$=$(5^{\rm h}35^{\rm m}14.^{\rm s}5, -5^{\circ}22'30.''4)$ and $(5^{\rm h}35^{\rm m}14.^{\rm s}5, -6^{\circ}00'30.''0)$. Each field was observed several times with azimuth and elevation scans. The separation among scans was adopted to be 117″, which is a quarter of the AzTEC field of view (FoV;$\sim 7.'8$). A scanning speed of the telescope was 250″ sec^{-1}. Totally 30 individual maps in the entire field with an integration time of 26 minutes were taken, and those maps were averaged to produce the final map with the total integration time of 26 minutes $\times$ 30 maps = 13 hours. The telescope pointing was checked every 2 hours by observing a quasar 0539-057 over a 4 $\times$ 4 arcmin^2 region. The derived pointing offsets were linearly interpolated along the time sequence and the interpolated pointing offset was applied to each target map. The pointing uncertainty of the AzTEC map is estimated to be better than 2″. We observed Uranus as a flux calibrator twice per night. By observing Uranus with each AzTEC detector element, we measured the flux conversion factor (FCF) from the optical loading value (in watts) to the source flux (in Jy beam^{-1}) for each detector element. The principal component analysis (PCA, Scott et al. 2008) cleaning method was applied to remove the atmospheric noise. Details of the flux calibration are described by Wilson et al. (2008) and Scott et al. (2008). Since the PCA method does not have sensitivity to extended sources, we apply the iterative mapping method (FRUIT, Liu et al. 2010) to recover the extended components. The noise level is $\sim$ 9 mJy beam^{-1} in the central region and $\sim$ 12 mJy beam^{-1} in the outer edge, the effective beam size is $\sim$ 40″, after the FRUIT imaging.

We describe the performance of FRUIT in appendix 1.

2.2. NRO 45m ^{12}CO (J=1–0) Line Observations

From December 2007 to May 2008, we carried out ^{12}CO (J=1–0; 115.271204 GHz) line observations toward the 1.°2 × 1.°2 region in the northern part of the Orion A molecular cloud with the 25-element focal plane receiver BEARS equipped in the 45 m telescope at NRO. At 115 GHz, the telescope has a FWHM beam size of 15″ and a main beam efficiency of 32 %. The beam separation of the BEARS is 41.″1 on the plane of the sky (Sunada et al. 2000; Yamaguchi et al. 2000). At the back end, we used 25 sets of 1024 channel auto-correlators (ACs) which have the bandwidth of 32 MHz and the frequency resolution of 37.8 kHz (Sorai et al. 2000). The frequency resolution corresponds to the velocity resolution of ~ 0.1 km s^{-1} at 115 GHz. During the observations, the system noise temperatures were in the range between 250 and 500 K in a double sideband. The standard chopper wheel method (Kutner & Ulich 1981) was used to convert the output signal into the antenna temperature $T_{\rm A}^{*}$ (K), corrected for the atmospheric attenuation. The telescope pointing was checked every 1.5 hours by observing a SiO maser source, Ori-KL, and was better than 3″ during the whole observing period. To correct the gain variation among the 25 beams of the BEARS, we used calibration data obtained from the observations toward Orion IRC 2 using another SIS receiver, S100, with a single sideband (SSB) filter and acousto-optical spectrometers (AOSs) as a back end.

Our mapping observations were made with the OTF mapping technique (Sawada et al. 2008). We used the emission-free area near ($\sim 2^{\circ}$ away) the observed area as the off position. We obtained an OTF map with a scanning direction both along the RA and DEC over the 1.°2 × 1.°2 region and combined them into a single map, in order to reduce the scanning effects. We adopted a convolutional scheme with a spheroidal function (Sawada et al. 2008) to calculate the intensity at each grid point of the final map-cube data with a spatial grid size of 7.″5, half of the beam size. The resultant effective resolution is 21″. The rms noise level of the final map is 0.94 K in $T_{\rm MB}$ (1 σ) at a velocity resolution of 1.0 km s^{-1}.

We summarize the parameters for the 1.1 mm continuum and the ^{12}CO (J=1–0) line observations in Table 1.

3. Results

3.1. 1.1 mm Dust Continuum Emission

Figure 1 shows the distribution of the 1.1 mm dust-continuum emission in the northern part of the Orion A molecular cloud. Previous observations of the northern part of the Orion A molecular cloud in dust-continuum emissions at 850 μm (Johnstone & Bally 1999; Nutter & Ward-Thompson 2007), 1.2 mm (Davis et al. 2009), and 1.3 mm (Chini et al. 1997) have revealed an "integral-shape" filamentary feature from the south to the north of Ori-KL (α_{J2000}, $\delta_{J2000} = 5^{\rm h}35^{\rm m}14.^{\rm s}5, -5^{\circ}22'30.''4$), where the northern end, region surrounding Ori-KL, and the

southern region of Ori-KL in the integral-shape filament are called OMC-2/3, OMC-1, and OMC-4, respectively. The global feature seen in our 1.1 mm dust-continuum map is consistent with that found in the previous observations, that is, the integral-shape filament along the north-south direction (named as "Integral-shape filament" in Figure 2). The central Orion-KL region has been masked out, because around the Ori-KL region the continuum emission is too bright to be reconstructed as an accurate structure with the AzTEC observing and data-reduction technique (see Appendix 1).

Our mapping area extends $\sim 1.^{\circ}7$ along the eastern and the western directions centered on the integral-shape filament, and is wider than that of the previous observations. As a result, we have found new dust-continuum features in the eastern and the western areas of the integral-shape filament, as described below.

3.1.1. New Features around the OMC-2/3 Region

Toward the east of the OMC-2/3 region, our high-sensitivity ($\sim$ 9 mJy) 1.1 mm continuum observations have revealed the presence of another filamentary structure (named as "new filament" in Figure 2). In addition, a continuum feature extending almost perpendicular to the integral-shape filament centered on MMS 9 (α_{J2000}, $\delta_{J2000} = 5^{\rm h}35^{\rm m}26.^{\rm s}00, -5^{\circ}05'42.''4$) was detected clearly at a signal to noise ratio of $\geq 50\ \sigma$, although this feature was not clearly seen in the previous studies (named as "east-west extension" in Figure 2). In the most eastern side of this structure, a cavity-like structure with a size of 0.4 pc was found at a central position of α_{J2000}, $\delta_{J2000} = 5^{\rm h}35^{\rm m}44^{\rm s}, -5^{\circ}06'48''$ (named as "cavity-shape" in Figure 2).

3.1.2. Features around the HII regions, M 42 and M 43

The distribution of the 1.1 mm dust-continuum emission around the HII region, M 43, which is excited by a B0.5 star, NU Ori (α_{J2000}, $\delta_{J2000} = 5^{\rm h}35^{\rm m}31.^{\rm s}36, -5^{\circ}16'02.''5$) (Thum et al. 1978), shows a shell-like structure with a size of $\sim$ 0.5 pc (named as "shell" in Figure 2). Toward the south of M 42 (OMC-4 region) the 1.1 mm dust-continuum emission shows a "V-shape" structure with a size of $\sim$ 2 pc, which is also seen in the 850 μm continuum emission (Johnstone & Bally 1999), and a cavity-like structure with a central position of (α_{J2000}, δ_{J2000} $= 5^{\rm h}35^{\rm m}13^{\rm s}, -5^{\circ}31'42''$)(named as "cavity" in Figure 2). Toward the northwest of M 42, the 1.1 mm dust-continuum emission forms an "L-shape" structure with a size of $\sim$ 0.5 pc (named as "L-shape" in Figure 2).

3.1.3. Filaments in peculiar shapes outside the integral filament

As well as the integral-shape filament there appears a branch of the 1.1 mm dust-continuum emission extending toward the southeast of Ori-KL. The branch forms a filamentary structure with a length of $\sim$ 3 pc along $\alpha_{J2000} \sim 5^{\rm h}36^{\rm m}$. This filament is known as one of photo-dominated regions (PDRs) from the CN line observations (Rodríguez-Franco et al. 2001) and is named as "dark lane south filament" (DLSF, named as "DLSF" in Figure 2). Furthermore, toward the opposite side of DLSF with respect to the integral-shape filament there is another filamentary structure with a size of $\sim$ 3 pc, which is bending at the middle (named as "Bending

structure" in Figure 2).

In the southmost region where an active cluster-forming region of L 1641 N (Chen et al. 1995; Chen et al. 1996; Stanke & Williams 2007) resides, four filamentary structures with a size of $\sim$ 0.5 - 2.0 pc are seen aligned almost in parallel (named as "paralleled filament" in Figure 2).

3.2. ^{12}CO (J=1–0) Emission

Figure 3 and 4 show the total integrated and the peak intensity maps of the ^{12}CO (J=1–0) emission in the northern part of the Orion A molecular cloud, respectively. The main feature seen in these maps is the same as that in the 1.1 mm continuum map, namely, integral-shape filament. At the eastern edge of the integral-shape filament there appears a sharp emission contrast while at the western edge the emission intensity decreases gradually. Hereafter we call the sharp emission contrast at the eastern edge of the integral-shape filament "CO front" (see Figure 5). In the total integrated intensity map the brightest point at the center corresponds to the location of Ori-KL. Toward the south-east of Ori-KL there appears a bar-like feature with a length of $\sim$ 0.6 pc, which is more evident in the peak intensity map. This feature corresponds to "Orion-Bar" (see Figure 5). As well as the ^{12}CO components associated with the integral-shape filament, there appears a branch of the ^{12}CO emission extending toward the southeast from Ori-KL. This ^{12}CO structure corresponds to DLSF seen in the AzTEC 1.1 mm dust-continuum emission (see Figure 5 as well as Figure 2). Similarly to CO front, there is a sharp emission contrast at the western side of DLSF. In addition to these filamentary features, a ^{12}CO emission extending to the east from Orion-KL and a diffuse CO emission at the west of the integral-shape filament are seen. These ^{12}CO emission features are consistent with the features found by the previous ^{12}CO (J=1–0) observations at an angular resolution of 45″ and a grid spacing of 45″ (Heyer et al. 1992). Toward the emission ridge, the peak intensity map of the ^{12}CO (J=1–0) emission probably shows the temperature structure, under the condition that the ^{12}CO (J=1–0) emission is optically thick and thermalized. The temperature around Ori-KL is the highest ($\sim$ 110 K), and the temperature around NGC 1977 is relatively high ($\sim$ 64 K).

Figure 6 shows the velocity channel maps of the ^{12}CO (J=1–0) emission with a velocity width of 1.0 km s^{-1}. In the high-velocity range ($V_{\rm LSR}$ = 2.5 - 3.5 & 15 - 18 km s^{-1}), a point-like ^{12}CO emission associated with Ori-KL is seen at (α_{J2000}, δ_{J2000}) = ($5^{\rm h}35^{\rm m}14\overset{\rm s}{.}5, -5^\circ22'30\overset{''}{.}4$). From $V_{\rm LSR}$ = 2.5 to 6.5 km s^{-1}, there is another compact ^{12}CO component seen toward the west of Ori-KL at (α_{J2000}, δ_{J2000}) = ($5^{\rm h}34^{\rm m}20\overset{\rm s}{.}4, -5^\circ22'24\overset{''}{.}2$). This ^{12}CO component is associated with the AzTEC 1.1 mm dusty condensation (named as "Region B", see §3.3). From $V_{\rm LSR}$ = 4.5 km s^{-1} to 14 km s^{-1} the main integral-shape filament shows a velocity gradient from the south to the north of Ori-KL, as already reported by previous observations (Bally et al. 1987; Heyer et al. 1992; Ikeda et al. 2007; Tatematsu et al. 2008). On the other hand, from $V_{\rm LSR}$ = 5.5 to

8.5 km s^{-1} the ^{12}CO emission originated from DLSF shows a velocity gradient from the north to the south (see Figure 5), which suggests that the velocity gradient of the ^{12}CO emission associated with DLSF is opposite compared to the large scale velocity gradient of the Orion A molecular cloud. The central velocity of DLSF ($\sim$ 7 km s^{-1}) is also different from that of the integral-shape filament. Hence, DLSF is likely to be kinematically distinct from the main cloud component. In the velocity range of 12 to 16 km s^{-1}, the ^{12}CO emission forms a shell-like structure with a size of $\sim$ 2 pc toward the south of Ori-KL (named as "shell around Ori-KL" in Figure 5). Bally et al. (1987) and Heyer et al. (1992) also found this shell-like structure around Ori-KL in the ^{13}CO (J=1–0) and the ^{12}CO (J=1–0) lines observations.

As well as these emission-ridge components, in the velocity range of 3.5 - 7.5 km s^{-1} there is extended diffuse CO component at the eastern region of the integral-shape filament. The peak intensity and the velocity width of the diffuse CO component are $\sim$ 5 K and $\sim$ 5 km s^{-1}, respectively. The origin of this rather featureless and extended ^{12}CO emission is likely to be different from that of the ridge components. Sakamoto et al. (1997) also found the diffuse CO component with a velocity width of $\sim$ 7 km s^{-1} and a peak intensity of $\sim$ 5 K in the east of the L 1641 N region, which locates in the southern part of the AzTEC 1.1 mm continuum map (Figure 1) and out of our ^{12}CO observing region. The diffuse CO component in the east of the L 1641 N region found by Sakamoto et al. (1997) is probably the same component as that in the east of the OMC-2/3 region and in the east of DLSF. Their and our results suggest that the diffuse CO component distributes along the east of the integral-shape filament over the extent of $\geq$ 14 pc. We will discuss the origin of the diffuse CO component in more detail.

Figure 3 shows the mean velocity map of the ^{12}CO (J=1–0) emission. The large-scale velocity gradient from the south to north can be confirmed in this mean velocity map as already shown in the channel maps (see Figure 6). Figure 4 shows the velocity dispersion map of the ^{12}CO (J=1–0) emission. The velocity dispersion map shows the increase of the velocity dispersion toward the east of CO front in the OMC-2/3 region (see Figure 5). Moreover, there is a shell-like structure around Ori-KL in the velocity dispersion map (see Figure 5).

3.3. Comparison Among the AzTEC 1.1 mm, ^{12}CO peak Intensity, 2MASS, and the MSX 8 μm Map

Figure 8 (a)-(d) show the AzTEC 1.1 mm, ^{12}CO (J=1–0) peak intensity, 2MASS, and the midcourse space experiment (MSX) 8 μm maps in the ^{12}CO observing region, respectively. The 8 μm emission mostly arises from polycyclic aromatic hydrocarbons (PAHs) and has been observed at the boundary of the HII regions (Zavagno et al. 2006). Recent laboratory experiments have shown that PAHs are produced on the dust grains irradiated by the FUV radiation (Bernstein et al. 1999). Hence, presence of the strong 8 μm emission suggests presence of the FUV radiation from HII regions. While the 1.1 mm and the ^{12}CO images show the distribution of the molecular gas, the 2MASS and the 8μm images show three bright nebulae, M 42, M

43, and NGC 1977. Although the millimeter and infrared emission distributions appear quite distinct from each other, detailed comparisons among the 1.1 mm, ^{12}CO, and the 8 μm images show their spatial correlations in several regions.

Figure 9 (a) and (b) compare the 1.1 mm continuum distribution to the MSX 8 μm and the ^{12}CO (J=1–0) emission distributions in the M 43 and DLSF region. In this region there are two HII regions, M 42 and M 43, excited by θ^1 Ori C and NU Ori, respectively. There are systematic trends of the 8 μm, 1.1 mm, and, the ^{12}CO emission distributions as a function of the distance from the HII regions. Toward M 43, there is a shell-like structure in the ^{12}CO, 1.1 mm, and the 8 μm emissions, however, the radius of the shell decreases systematically from the ^{12}CO, 1.1 mm, and the 8 μm emissions. DLSF is likely to be irradiated by θ^1 Ori C and the ^{12}CO, 1.1 mm, and the 8 μm emissions show systematic emission distributions as a function of the distance from θ^1 Ori C; the ^{12}CO emission distribution is located farthest and the 8 μm closest.

We have also identified other four regions with the systematic ^{12}CO, 1.1 mm, and the 8 μm emissions distribution. These regions are labeled as Region A-D, and the locations of Region A-D are shown in Figure 5.

Figure 10 - 13 show the same maps as those in Figure 9 but for Region A-D, respectively.

In Region A where the 1.1 mm continuum peak locates at (α_{J2000}, δ_{J2000})=($5^{\rm h}34^{\rm m}35\overset{\rm s}{.}5, -5°18'05\overset{''}{.}3$), the nearest ($d$= $\sim$ 1.4 pc) HII region, M 42, is located on the southeast from the continuum peak (see an arrow in Figure 10). The 8 μm, 1.1 mm, and the ^{12}CO emissions show the systematic distributions along the direction to the HII region; The 8 μm emission distributes on the southeastern part of the 1.1 mm dust-continuum condensation, while the ^{12}CO emission distributes on the central part of the 1.1 mm dust-continuum condensation.

In Region B where the 1.1 mm continuum peak locates at (α_{J2000}, δ_{J2000})=($5^{\rm h}33^{\rm m}57\overset{\rm s}{.}4, -5°23'28\overset{''}{.}9$), the nearest ($d$= $\sim$ 2.3 pc) HII region, M 42, is located on the east from the continuum peak (see an arrow in Figure 11). The 8 μm and the ^{12}CO emissions show the positional offset along the direction to the HII region, and the 8 μm emission locates on the side of the HII region. The dusty condensation in Region B is associated with a Spitzer 24 μm source.

In Region C where the 1.1 mm continuum peak locates at (α_{J2000}, δ_{J2000})=($5^{\rm h}33^{\rm m}49\overset{\rm s}{.}9, -5°39'00\overset{''}{.}1$), the nearest ($d$= $\sim$ 3.2 pc) HII region, M 42, is located on the north from the continuum peak (see an arrow in Figure 12). The 8 μm, ^{12}CO, and the 1.1 mm emissions show the systematic distributions along the direction to the HII region; The 8 μm emission distributes on the northern part of the 1.1 mm dust-continuum condensation, while the ^{12}CO emission distribution is similar to the 1.1 mm emission distribution.

In Region D where the 1.1 mm continuum peak locates at (α_{J2000}, δ_{J2000})=($5^{\rm h}35^{\rm m}30\overset{\rm s}{.}5, -5°40'06\overset{''}{.}5$), the nearest ($d$= $\sim$ 2.0 pc) HII region, M 42, is located

on the north from the continuum peak (see an arrow in Figure 13). The 8 μm, 1.1 mm, and the ^{12}CO emissions show the systematic distributions along the direction to the HII region; The 8 μm emission distributes on the northern part of the 1.1 mm dust-continuum condensation, while the ^{12}CO emission distributes on the southern part of the 1.1 mm dust-continuum condensation.

4. Discussion

4.1. Large Scale Possible External Effect; Collision of the Diffuse Components on the Cloud Surface

One of the first findings in our extensive ^{12}CO (J=1–0) emission observations of the northern part of the Orion A molecular cloud is the presence of the diffuse CO component over the entire eastern region of the integral-shape filament. Figure 14 highlights the total integrated intensity map of the diffuse CO component with respect to the peak intensity map at the OMC-2/3 region, and Figure 15 shows position - velocity (P-V) diagrams whose cut lines are along the RA direction shown in Figure 14. In the P-V diagrams, the central velocity of the diffuse CO component is 5 - 6 km s^{-1}, while that of the main component is 11 - 12 km s^{-1}. These two velocity components appear to be connected at CO front, raising the ^{12}CO velocity dispersion at CO front. Figure 16 shows peak intensity profiles whose cut lines are the same as that of the P-V diagrams in Figure 15. While the peak intensity of the diffuse CO component is around 4 - 7 K at $T_{\rm MB}$, that of the main cloud component exceeds 50 K, and hence there is an abrupt increase of the ^{12}CO peak intensity at CO front. In contrast, toward the western outskirts of the main cloud component the ^{12}CO peak intensity decreases gradually (see Figure 3 - 5). These peculiar features extend over the entire CO front as can be seen in Figures 3 - 6, although toward the southern part of CO front the difference of the central velocities becomes smaller. The reason why the velocity difference between the diffuse CO component and the main cloud component becomes less clear is the large scale velocity gradient of the main cloud component (see §3.2).

There are two possible interpretations on the origin of the diffuse CO component; One is the trail of the main cloud component moving away from the galactic plane and the other is the pre-existing surrounding diffuse gas swept up by neighboring external sources. Sakamoto et al. (1997) has suggested these two possibilities on the origin of the diffuse CO component in the east of the L 1641 N region. It is, however, difficult to explain the difference of the central velocity between the diffuse CO component and the main cloud component and the abrupt increase of the ^{12}CO peak intensity by the former interpretation. We consider that the "L-shaped" feature of the diffuse CO component in the P-V diagrams and the abrupt increase of the ^{12}CO peak intensity imply presence of the interaction between the diffuse CO component and the main cloud component (Takakuwa et al. 2003; Shimajiri et al. 2008), and that the diffuse

CO component is being accumulated on to the surface of the main cloud component at CO front. In fact, Bally et al. (1987), Lee & Chen (2009) and Wilson et al. (2005) have suggested that Ori OB 1a and Ori OB 1b, $\sim$ 100 pc away from the Orion A molecular cloud, affect the Orion A molecular cloud and disturb the morphology and kinematics of the cloud, respectively. These OB stars are the possible sources to sweep up the pre-existing diffuse material toward the direction to the main cloud component. Our observational results favor the proposal by Wilson et al. (2005), since Ori OB 1b locates in the east of the Orion A molecular cloud and the diffuse CO component also distributes toward the same direction from the Orion A molecular cloud. The collision of the diffuse CO component with the main cloud component might trigger the next star formation in the cloud (Lada 1987).

4.2. Intermediate Scale Possible External Effect; Photo-Dominated Regions

In the last section, we suggest the possibility that the diffuse CO component is swept up by Ori OB 1b and interacts with the entire Orion A molecular cloud. In this section, we focus on more local effects in a few pc-scale, namely, the HII regions embedded in the Orion A molecular cloud. As well as the external sources away from the cloud, newly born OB stars embedded in the cloud can also influence on the structure, chemistry, thermal balance, and the star formation in the cloud (Hollenbach & Tielens 1997). There are several OB stars (such as θ^1 Ori C and NU Ori) and HII regions in our mapping area of the Orion A molecular cloud and these sources are likely to affect star formation in the Orion A molecular cloud. As shown in §3.3, we found that there are systematic differences of the distribution among the ^{12}CO, 1.1 mm, and the 8 μm emissions and that the 8 μm, 1.1 mm, and the ^{12}CO emissions are distributed as a function of the distance from the OB stars. The most clear example is in DLSF irradiated by θ^1 Ori C, and the intensity profiles as a function of the distance from θ^1 Ori C are shown in Figure 17.

The presence of the strong 8 μm emission suggests the FUV radiation from the HII regions. On the other hand, ^{12}CO molecules are dissociated by the FUV radiation, since the energy of FUV (6 eV - 13.6 eV) is high enough to dissociate ^{12}CO molecules with an dissociative energy of 11.4 eV. Hence, the ^{12}CO emission does not distribute at the near side of the exciting star. The 1.1 mm emission traces both the cold and warm dusts. Hence, the systematic distributions of the 8 μm, 1.1 mm, and the ^{12}CO emissions can be explained by the PDR model (Hollenbach & Tielens 1997). In fact, toward DLSF and M 43, where the systematic distributions of the ^{12}CO, 1.1 mm, and the 8 μm emissions are seen, the observations of the CN line, one of the excellent tracers for PDR, suggest the presence of PDR.

Region A-D, relatively isolated dusty condensations, also exhibit the systematic distributions of the ^{12}CO, 1.1 mm, and the 8 μm emissions along the direction to the exciting sources. These isolated condensations are likely to be pre-existing molecular cloud cores. When an expanding HII region interacts with a pre-existing molecular cloud core, the strong UV radiation

will compress the core. This compression could induce the gravitational collapse of the core (Bertoldi 1989; Motoyama et al. 2007). Our results suggest that the dusty condensations of Region A-D are affected by the UV radiation from the OB stars. Moreover, the dusty condensation of Region B is associated with the spitzer 24 μm sources, suggesting the presence of the star formation.

5. Summary

We have carried out extensive mapping observations of the northern part of the Orion A molecular cloud in the 1.1 mm dust-continuum emission with the AzTEC camera equipped in the ASTE telescope and in the ^{12}CO (J=1–0) emission with the BEARS receiver equipped in the NRO 45 m telescope. The main results of our wide-field ($1.^{\circ}7 \times 2.^{\circ}3$) and high-sensitivity ($\sim$ 9 mJy beam^{-1}) observations are summarized as follows;

1. We have found new features of the 1.1 mm dust-continuum emission in addition to the previously known integral-shape filament. In the OMC-2/3 region, a new dusty filamentary structure is detected toward the east of the integral-shape filament. A dusty shell-like structure around the HII region, M 43, and a filamentary structure associated with DLSF are detected. In the southmost region where an active cluster-forming region of L 1641 N is located, four filamentary structures with a size of $\sim$ 0.5 - 2.0 pc are seen aligned almost in parallel.
2. In the ^{12}CO (J=1–0) line observations, we found diffuse CO component over the entire eastern region of the integral-shape filament. The peak intensity profiles from the diffuse CO component to the integrals-shape filament show an abrupt increase at the border line (CO front) and the P-V diagrams show the sudden velocity change from 5 - 6 km s^{-1} to 11- 12 km s^{-1}. We suggest that these peculiar features of the diffuse CO component show that the diffuse material swept up by Orion OB 1b, $\sim$100 pc away from the Orion A molecular cloud, is being accumulated onto the surface of the integral-shape filament.
3. Comparisons among the ^{12}CO, 1.1 mm, and the 8 μm emission distribution in M 43, DLSF, and Region A-D have revealed that the 8 μm, 1.1 mm, and the ^{12}CO emissions are located sequentially as a function of the distance from the neighboring OB stars. These results suggest the presence of the PDRs around M 43, DLSF, and Region A-D, excited by the NU Ori, θ^1 Ori C, and θ^1 Ori C, respectively. In particular, the dusty condensation of Region B is associated with a Spitzer 24 μm source, suggesting the presence of the star formation. Region A-D are possible site of star formation triggered by the PDRs.

We thank the referee, Charles Lada, for his constructive comments that polish the manuscript significantly. We are grateful to the staffs at the Nobeyama Radio Observatory (NRO) for both operating the 45 m and helping us with the data reduction, and to NRO is a branch of the National Astronomical Observatory, National Institutes of Natural Sciences,

Japan. We also acknowledge the ASTE staffs for both operating ASTE and helping us with the data reduction. Observations with ASTE were (in part) carried out remotely from Japan by using NTT's GEMnet2 and its partner R&E (Research and Education) networks, which are based on AccessNova collaboration of University of Chile, NTT Laboratories, and National Astronomical Observatory of Japan. This research has made use of the NASA/ IPAC Infrared Science Archive, which is operated by the Jet Propulsion Laboratory, California Institute of Technology, under contract with the National Aeronautics and Space Administration. This work was supported by Grant-in-Aid for Scientific Research A 18204017. Y. Shimajiri is financially supported by a Research Fellowship from the JSPS for Young Scientists.

Appendix 1. AzTEC Data Reduction & Performance

In this appendix, we present our imaging simulation with artifact gaussian sources as input models, in order to test the performance of the AzTEC data reduction.

A.1.1. AzTEC Data Reduction

The AzTEC data set is reduced by using the available AzTEC data reduction pipeline written in IDL and developed by the University of Massachusetts according to guidelines in Scott et al. (2008). This pipeline includes the despiking, atmosphere removal, and optimal filtering. The despiking which is removal of the cosmic ray is, however, not applied to Orion data reduction to avoid the removal of source emission, since the emission in the Orion region is too strong. Principal components analysis (PCA) cleaning method is applied for removal of the atmospheric noise in this pipeline. Finally, the 30 individual maps were coadded. This data reduction pipeline has, however, been optimized for the identification of point sources. The PCA cleaning removes the astronomical signals in the case that the emission has an extended structure, since the signals which are a good correlation among each element are regarded as the atmospheric components and are removed. Hence, the flux and size of the extended sources are underestimated. In order to recover the extended features in the Orion map which is subtracted by the PCA cleaning, we apply an iterative mapping method to the Orion data-set. Hereafter, we call this method, FRUIT. This method is based on an iterative mapping method applied to the BOLOCAM data reduction pipeline (Enoch et al. 2006). The FRUIT data reduction pipeline is also written in IDL and developed by the University of Massachusetts. The FRUIT algorithm is described in Liu et al. (2010).

A.1.2. Performance of FRUIT

In order to investigate the performance of FRUIT, we have performed the simulation that the twenty five gaussian sources with a peak flux of 1 Jy and a FWHM size of 30, 60, 90, 120, 150, and 180″ are inserted to Orion data-set and are applied the data reduction pipeline. Figure 18 shows the fraction of the over-estimated (positive) or missed (negative) flux,

$(\frac{\text{output total flux}}{\text{input total flux}} - 1) \times 100$, as a function of the FWHM size of the input model Gaussian. We have applied the aperture photometry to estimate the total flux. Error bars show a standard deviation (1 σ) of the output total flux among twenty five sources. In the case that the FWHM size of the input model Gaussian is under 150″, the output total flux is underestimated by less than 20%. The total-flux reproductivity of the source with larger FWHM is lower than that with smaller FWHM. We insert the twenty five sources with a peak flux of 1, 20, 40, 60, and 80 Jy and a FWHM size of 60″ to the Orion data-set and applies the same data reduction pipeline. Figure 19 shows the fraction of the over-estimated (positive) or missed (negative) flux as a function of the peak flux of the input model Gaussian. The total flux of sources with a peak flux under 20 Jy is underestimated by less than 10 %. The reproductivity of the total flux is, however, low for the source with a peak flux over 20 Jy. In the case of Orion, the total flux of sources in our map should be recovered by more than 80 %, since the peak flux and the FWHM size of most sources are smaller than 20 Jy and 150″. Moreover, the restored image of the 1.1 mm dust continuum emission is consistent with that of the SCUBA 850 μm dust continuum emission as shown in Figure 20.

References

Aso, Y., Tatematsu, K., Sekimoto, Y., Nakano, T., Umemoto, T., Koyama, K., & Yamamoto, S. 2000, ApJS, 131, 465

Bally, J., Lanber, W. D., Stark, A. A., & Wilson, R. W. 1987, ApJL, 312, L45

Bertoldi, F. 1989, ApJ, 346, 735

Bernstein, M. P., Sandford, S. A., Allamandola, L. J., Gillette, J. S. B., Clemett, S. J.,& Zare, R. N. 1999, Science, 283, 1135

Chen, H., Zhao, J.-H., & Ohashi, N. 1995, ApJL, 450, L71

Chen, H., Ohashi, N., & Umemoto, T. 1996, AJ, 112, 717

Chini, R., Reipurth, B., Ward-Thompson, D., Bally, J., Nyman, L.-A., Sievers, A., & Billawala, Y. 1997, ApJL, 474, L135

Cowie, L. L., Songaila, A., & York, D. G. 1979, ApJ, 230, 469

Davis, C. J., et al. 2009, A&A, 496, 153

Elmegreen, B. G. 1998, Origins, 148, 150

Enoch, M. L., et al. 2006, ApJ, 638, 293

Ezawa, H., Kawabe, R., Kohno, K., & Yamamoto, S. 2004, Proc. SPIE, 5489, 763

Goudis: 1982, $The Orion complex : a case study of interstellar matter, D. Reidel Publishing Company$

Heyer, M. H., Morgan, J., Schloerb, F. P., Snell, R. L., & Goldsmith, P. F. 1992, ApJL, 395, L99

Hirota, T., et al. 2008, PASJ, 60, 961

Hollenbach, D. J., & Tielens, A. G. G. M. 1997, ARA&A, 35, 179

Homeier, N. L., & Alves, J. 2005, A&A, 430, 481

Hosokawa, T., & Inutsuka, S.-i. 2005, ApJ, 623, 917

Ikeda, N., Sunada,K., & Kitamura, Y. 2007, ApJ, 665, 1194

Johnstone, D., & Bally, J. 1999, ApJL, 510, L49
Kohno, K., et al. 2004, The Dense Interstellar Medium in Galaxies, 349
Kutner, M. L., & Ulich, B. L. 1981, ApJ, 250, 341
Lada, C. J. 1987, Star Forming Regions, 115, 1
Lada, C. J., & Lada, E. A. 2003, ARA&A, 41, 57
Lee, H.-T., & Chen, W. P. 2009, ApJ, 694, 1423
Lis, D. C., Serabyn, E., Keene, J., Dowell, C. D., Benford, D. J., Phillips, T. G., Hunter, T. R., & Wang, N. 1998, ApJ, 509, 299
Liu, G., et al. 2010, AJ, 139, 1190
Megeath, S. T. 1994, The Structure and Content of Molecular Clouds, 439, 215
Menten, K. M., Reid, M. J., Forbrich, J., & Brunthaler, A. 2007, A&A, 474, 515
Momose, M., Ohashi, N., Kawabe, R., Nakano, T., & Hayashi, M. 1998, ApJ, 504, 314
Motoyama, K., Umemoto, T., & Shang, H. 2007, A&A, 467, 657
Myers, P. C., Bachiller, R., Caselli, P., Fuller, G. A., Mardones, D., Tafalla, M., & Wilner, D. J. 1995, ApJL, 449, L65
Nakamura, F., & Li, Z.-Y. 2007, ApJ, 662, 395
Nutter, D., & Ward-Thompson, D. 2007, MNRAS, 374, 1413
Rodríguez-Franco, A., Wilson, T. L., Martín-Pintado, J., & Fuente, A. 2001, ApJ, 559, 985
Sakamoto, S., Hasegawa, T., Hayashi, M., Morino, J.-I., & Sato, K. 1997, ApJ, 481, 302
Sandell, G., & Knee, L. B. G. 2001, ApJL, 546, L49
Saito, M., Sunada, K., Kawabe, R., Kitamura, Y., & Hirano, N. 1999, ApJ, 518, 334
Sandstrom, K. M., Peek, J. E. G., Bower, G. C., Bolatto, A. D., & Plambeck, R. L. 2007, ApJ, 667, 1161
Sawada, T., et al. 2008, PASJ, 60, 445
Scott, K. S., et al. 2008, MNRAS, 385, 2225
Shimajiri, Y., Takahashi, S., Takakuwa, S., Saito, M., & Kawabe, R. 2008, ApJ, 683, 255
Shimajiri, Y., Takahashi, S., Takakuwa, S., Saito, M., & Kawabe, R. 2009, PASJ, 61, 1055
Solomon, P. M., Sanders, D. B., & Scoville, N. Z. 1977, BAAS, 9, 554
Sorai, K., Sunada, K., Okumura, S. K., Tetsuro, I., Tanaka, A., Natori, K., & Onuki, H. 2000, Proc. SPIE, 4015, 86
Stanke, T., McCaughrean, M. J., & Zinnecker, H. 2002, A&A, 392, 239
Stanke, T., & Williams, J. P. 2007, AJ, 133, 1307
Sunada, K., Yamaguchi, C., Nakai, N., Sorai, K., Okumura, S. K., & Ukita, N. 2000, Proc. SPIE, 4015, 237
Takahashi, S., Saito, M., Ohashi, N., Kusakabe, N., Takakuwa, S., Shimajiri, Y., Tamura, M., & Kawabe, R. 2008, ApJ, 688, 344
Takahashi, S., Ho, P. T. P., Tang, Y.-W., Kawabe, R., & Saito, M. 2009, ApJ, 704, 1459
Takakuwa, S., Ohashi, N., & Hirano, N. 2003, ApJ, 590, 932
Takakuwa, S., et al. 2004, ApJL, 616, L15
Tatematsu, K., et al. 1993, ApJ, 404, 643

Tatematsu, K., Umemoto, T., Heyer, M. H., Hirano, N., Kameya, O., & Jaffe, D. T. 1998, ApJS, 118, 517

Tatematsu, K., Kandori, R., Umemoto, T., & Sekimoto, Y. 2008, PASJ, 60, 407

Thum, C., Lemke, D., Fahrbach, U., & Frey, A. 1978, A&A, 65, 207

Tsujimoto, M., Koyama, K., Tsuboi, Y., Goto, M., & Kobayashi, N. 2002, ApJ, 566, 974

Whitworth, A. P., Bhattal, A. S.,Chapman, S. J., Disney, M. J., & Turner, J. A. 1994, A&A, 290, 421

Wilson, B. A., Dame, T. M., Masheder, M. R. W., & Thaddeus, P. 2005, A&A, 430, 523

Wilson, G. W., et al. 2008, MNRAS, 386, 807

Yamaguchi, C., Sunada, K., Iizuka, Y., Iwashita, H., & Noguchi, T. 2000, Proc. SPIE, 4015, 614

Yokogawa, S., Kitamura, Y., Momose, M., & Kawabe, R. 2003, ApJ, 595, 266

Yonekura, Y., Asayama, S., Kimura, K., Ogawa, H., Kanai, Y., Yamaguchi, N., Barnes, P. J., & Fukui, Y. 2005, ApJ, 634, 476

Zavagno, A., Deharveng, L., Comerón, F., Brand, J., Massi, F., Caplan, J., & Russeil, D. 2006, A&A, 446, 171

Zinnecker, H., & Yorke, H. W. 2007, ARA&A, 45, 481

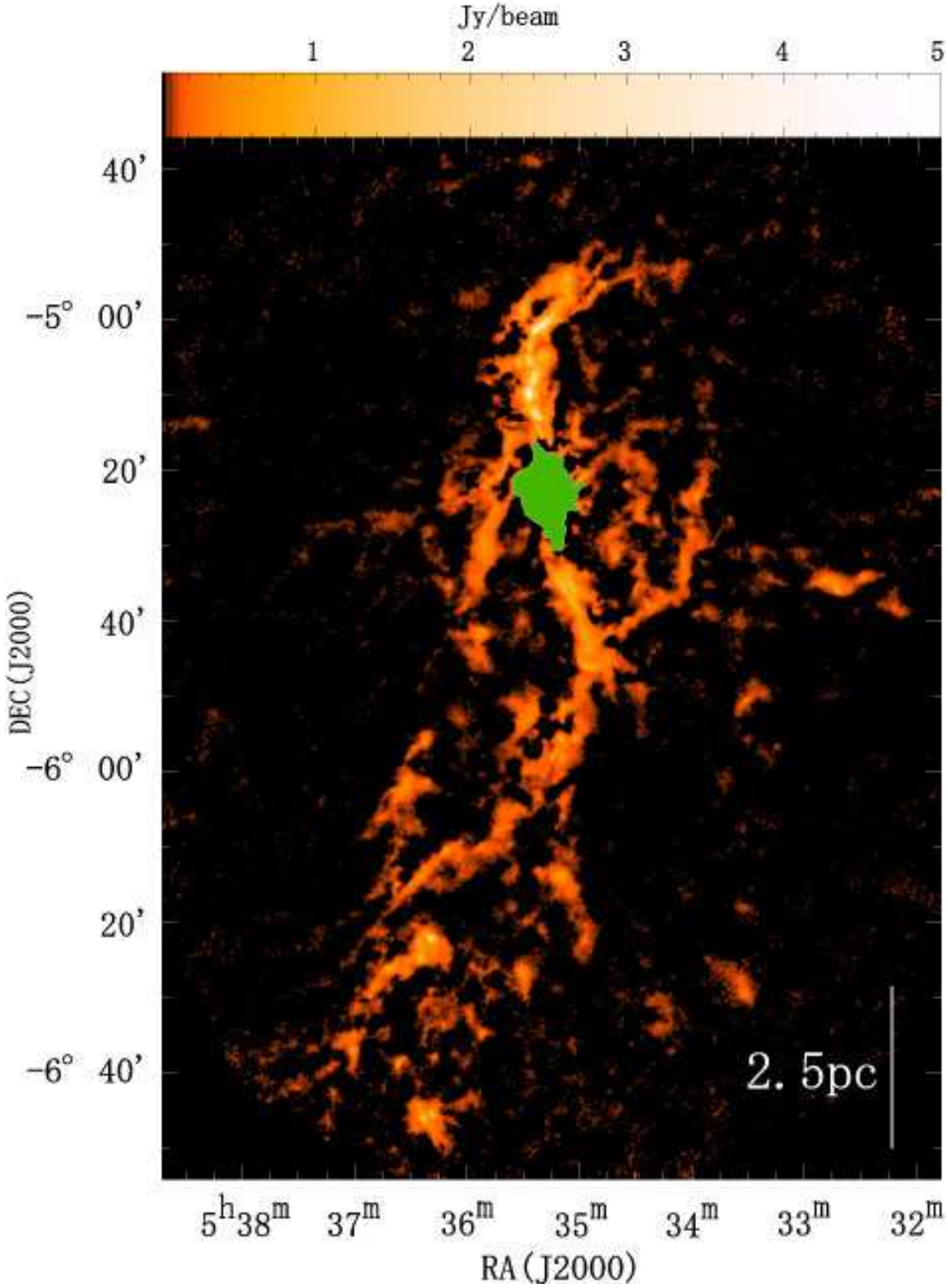

Fig. 1. AzTEC/ASTE 1.1 mm dust continuum map. The rms noise level is 9 mJy beam^{-1} in the central region and 12 mJy beam^{-1} on the outer edge. The central Orion-KL region has been masked out for this analysis, because the continuum emission around Orion-KL is too bright to be reconstructed as an accurate structure with the AzTEC data-reduction technique.

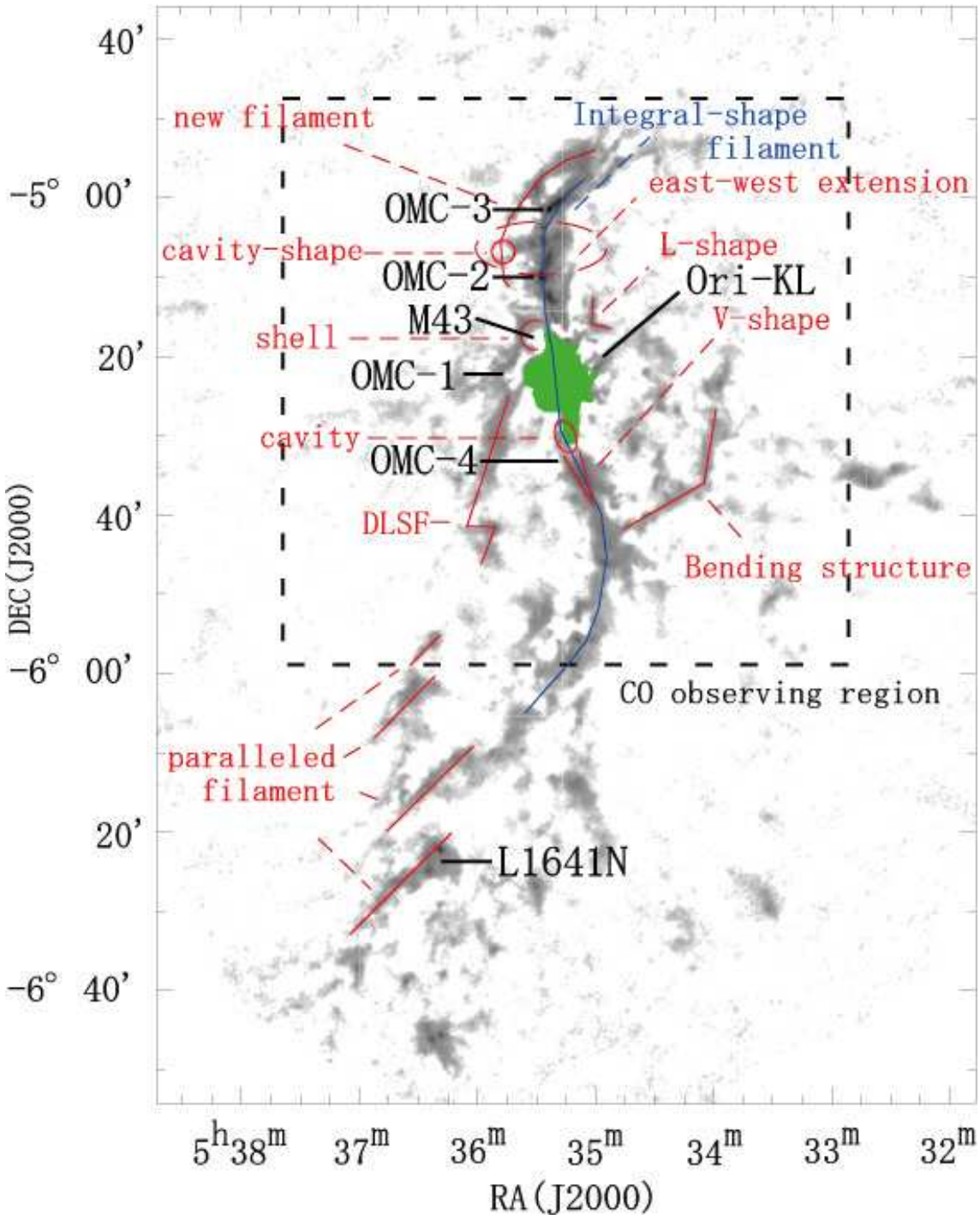

Fig. 2. Map of main 1.1 mm dust continuum features. The details of the features are described in section 3.1. A black box, $\sim 1.2 \times \sim 1.2$ degree^2 in size, shows the ^{12}CO (J=1–0) observing region. The central Orion-KL region has been masked out for this analysis, because the continuum emission around Orion-KL is too bright to be reconstructed as an accurate structure with the AzTEC data-reduction technique.

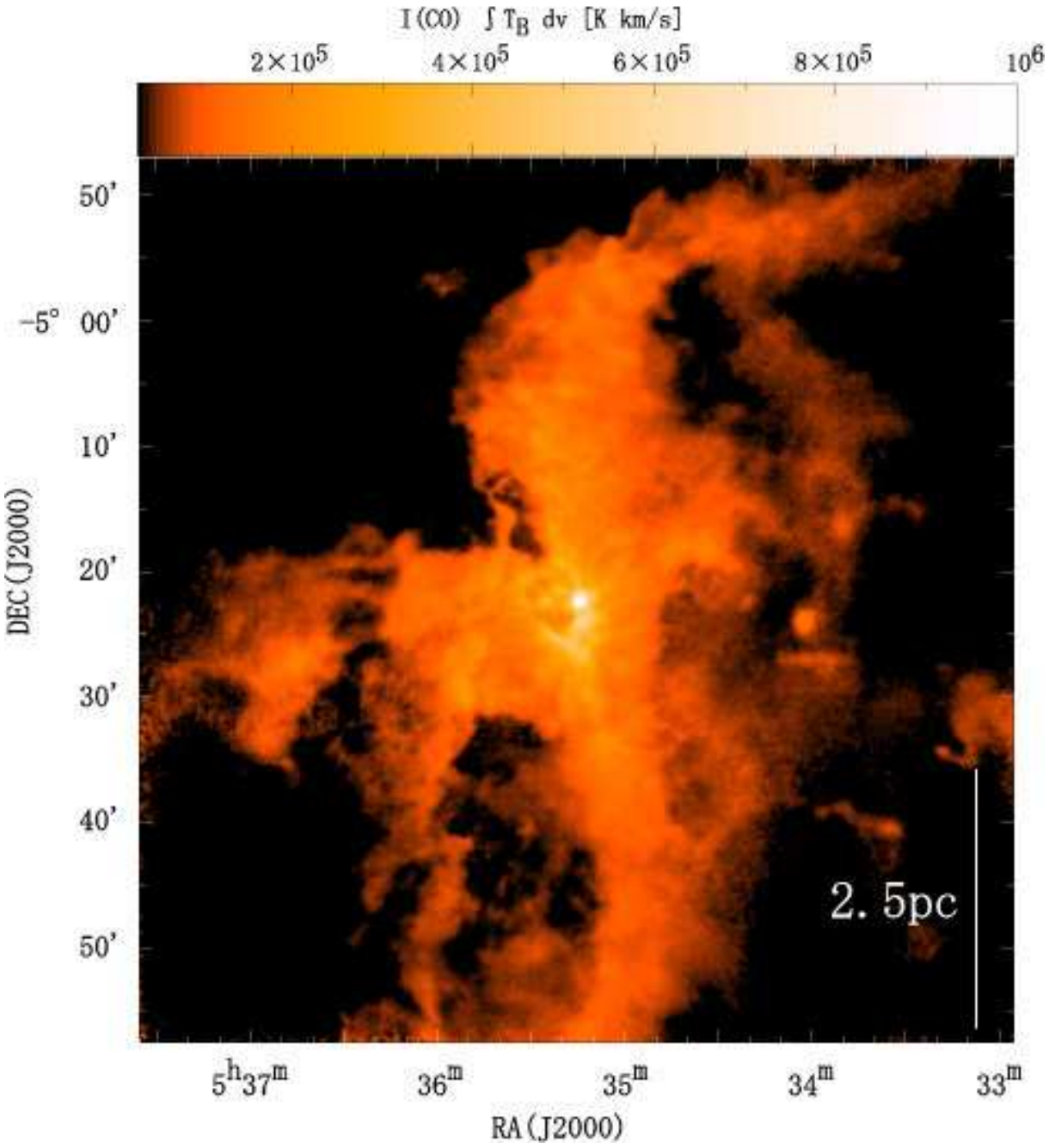

Fig. 3. ^{12}CO (J=1–0) total integrated intensity map at a velocity range of 0.0 - 20.0 km s^{-1}. The noise level (1 σ) is 70.0 K km s^{-1}, and the peak intensity is $\sim 1.62 \times 10^7$ K km s^{-1}.

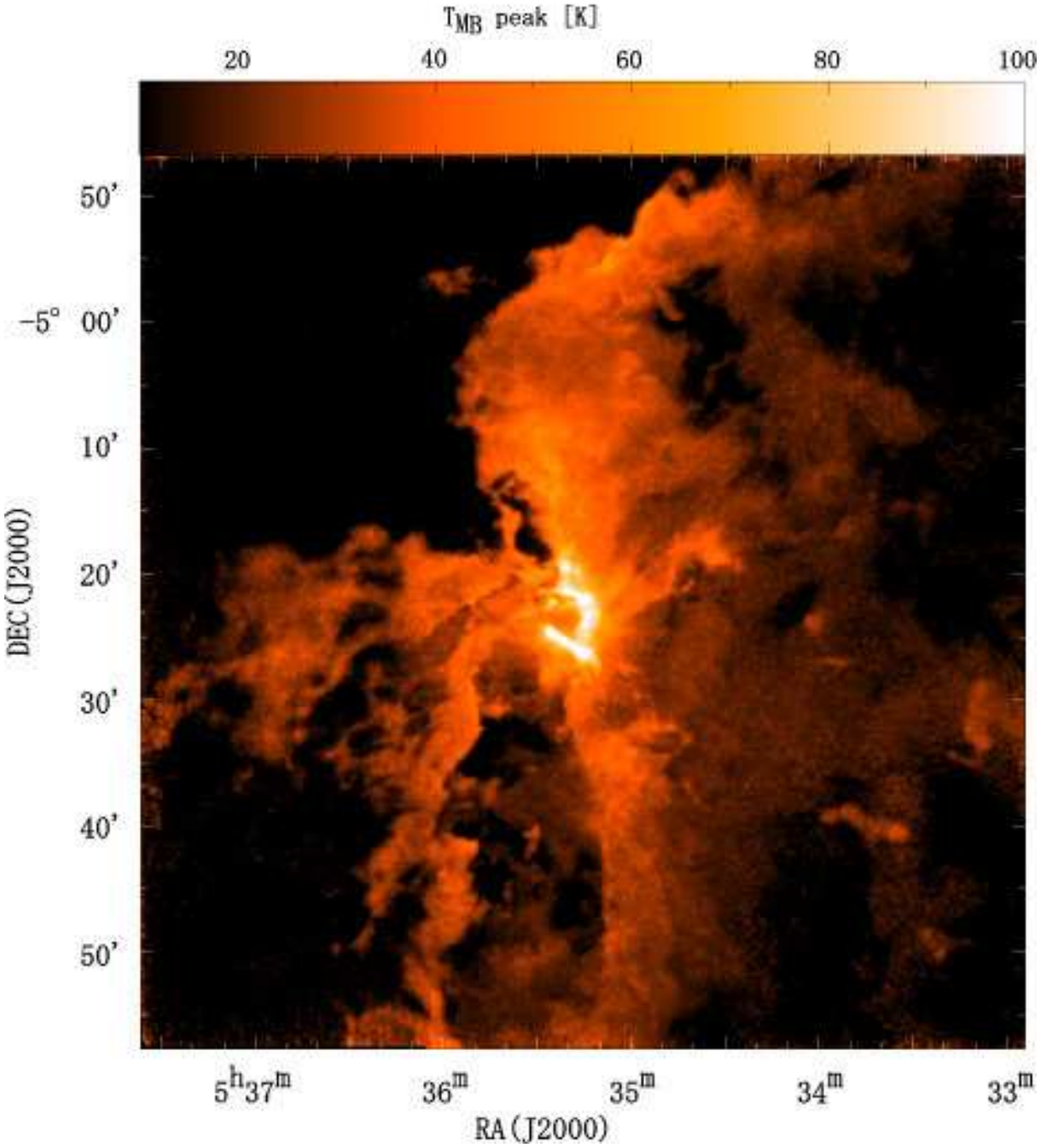

Fig. 4. Peak intensity map in the ^{12}CO (J=1–0) line. The noise level (1 σ) is 1.4 K at $T_{\rm MB}$ and the peak intensity is $\sim$ 111.7 K at $T_{\rm MB}$.

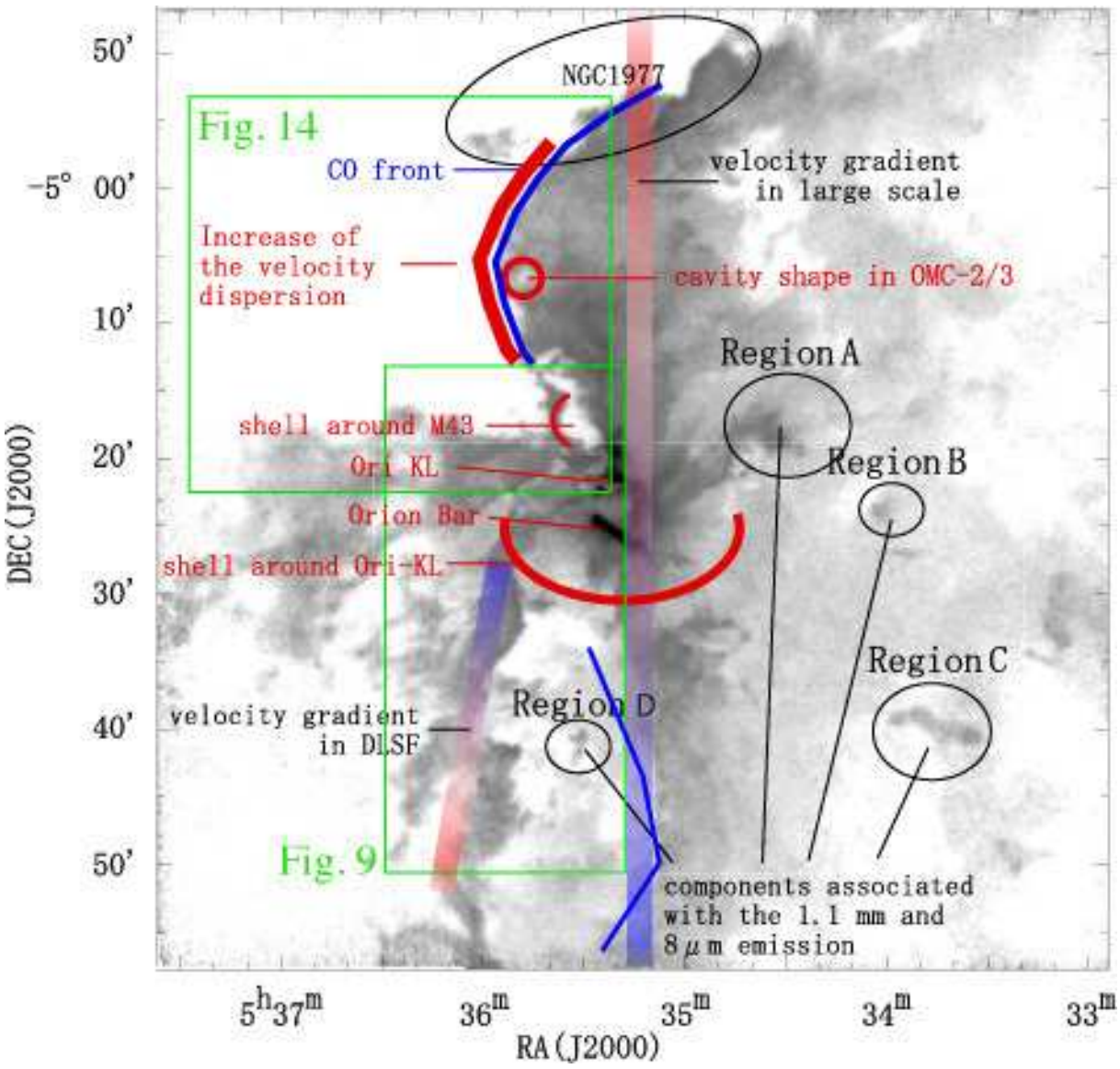

Fig. 5. Map of ^{12}CO (J=1–0) emission features. Grey scale is a peak intensity map in the ^{12}CO (J=1–0) line. The detail of the features are described in section 3.2.

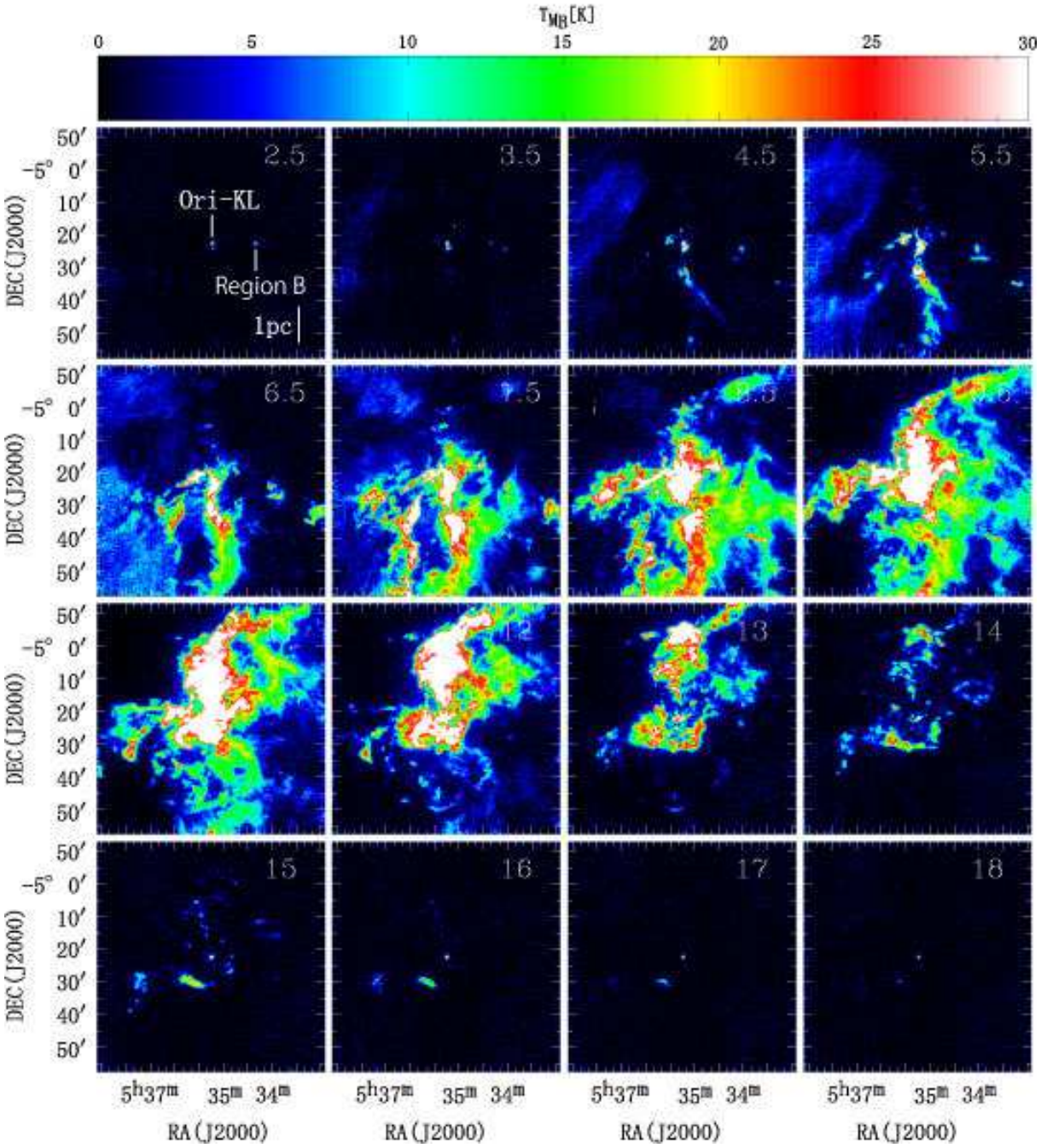

Fig. 6. ^{12}CO (J=1–0) velocity channel maps. The image size is $\sim 1.2 \times 1.2$ degree^2, and the effective special resolution is $\sim$21″. The velocity width of each map is 1.0 km s^{-1}, and typical noise level (1 σ) is 0.93 K in $T_{\rm MB}$.

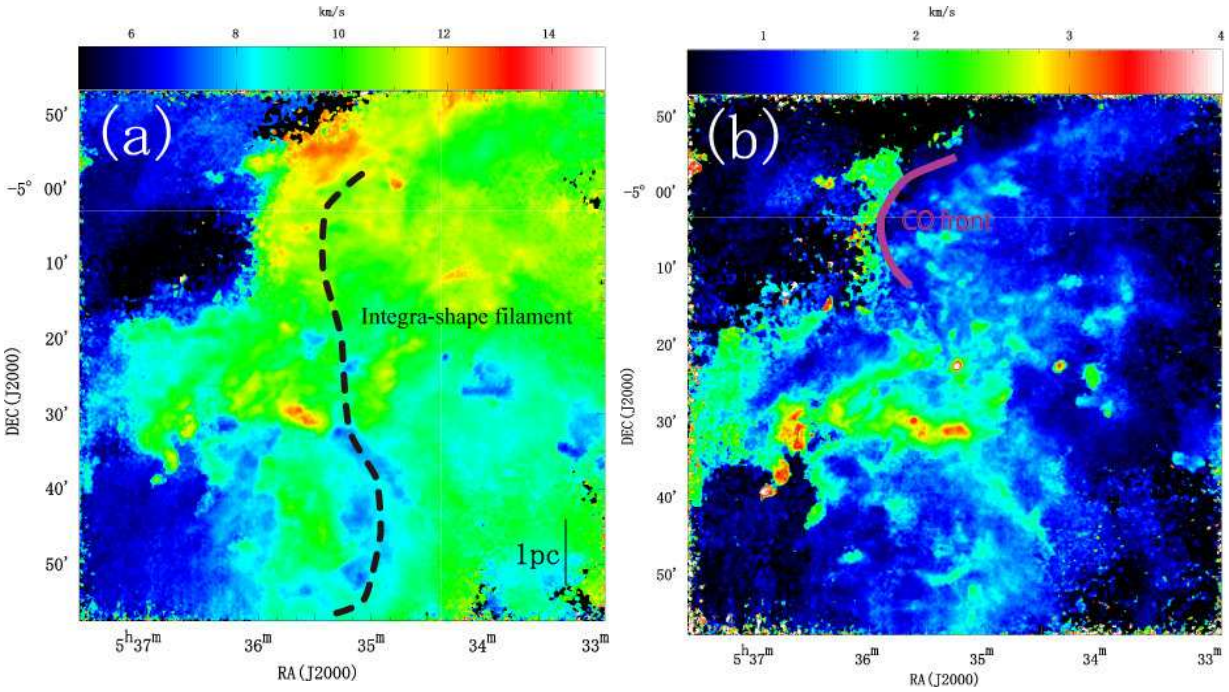

Fig. 7. (a) ^{12}CO intensity-weighted mean velocity map at a velocity range of 0.0 - 20.0 km s^{-1}. Blue, green, and yellow colors show the $\leq$ 9.0, 9.0 - 11.0 , $\geq$ 11.0 km s^{-1}, respectively. (b) ^{12}CO velocity dispersion map at a velocity range of 0.0 - 20.0 km s^{-1}. Blue, green, and yellow colors shows the $\leq$ 1.6, 1.6 - 2.8, $\geq$ 2.8 km s^{-1}, respectively.

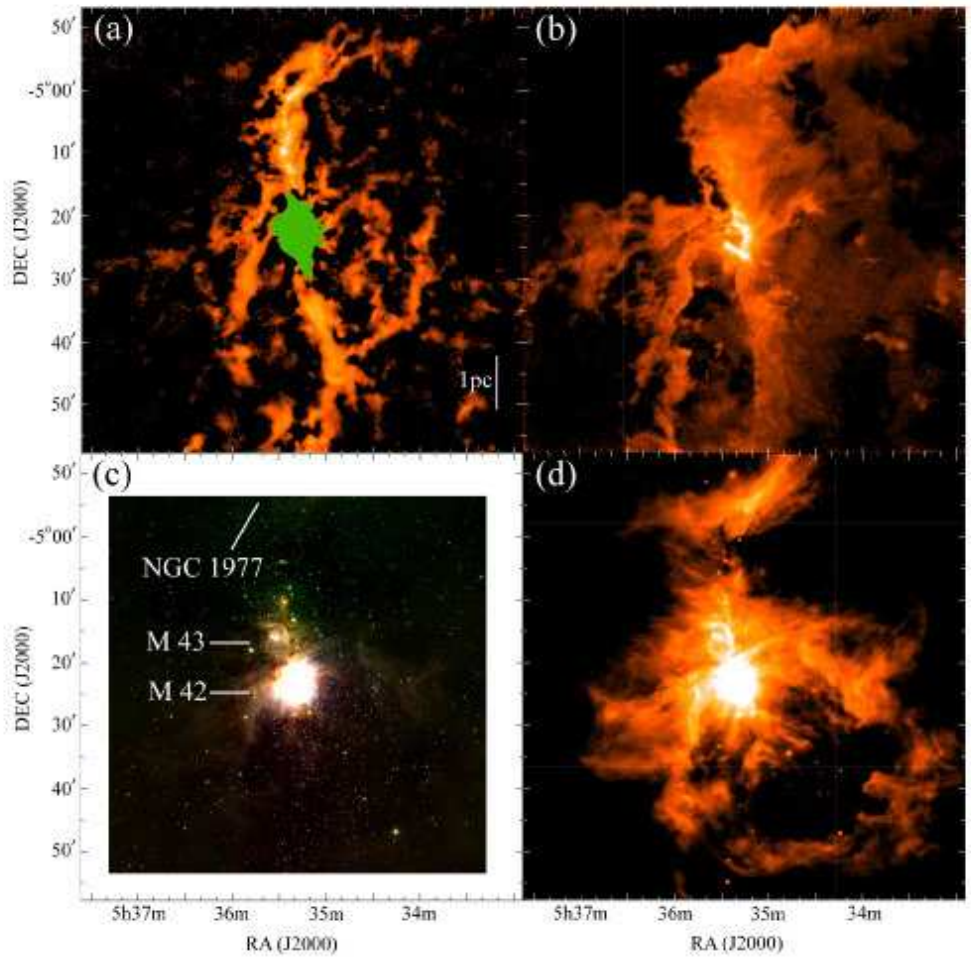

Fig. 8. (a) AzTEC/ASTE 1.1 mm dust-continuum image. The central Orion-KL region has been masked out for this analysis, because the continuum emission around Orion-KL is too bright to be reconstructed as an accurate structure with the AzTEC data-reduction technique. (b) peak intensity map in the ^{12}CO (J=1–0) line (c) 2MASS image obtained from the archive of IPAC image mosaic service. (d) MSX 8 μm image obtained from the archive of IRAC Services.

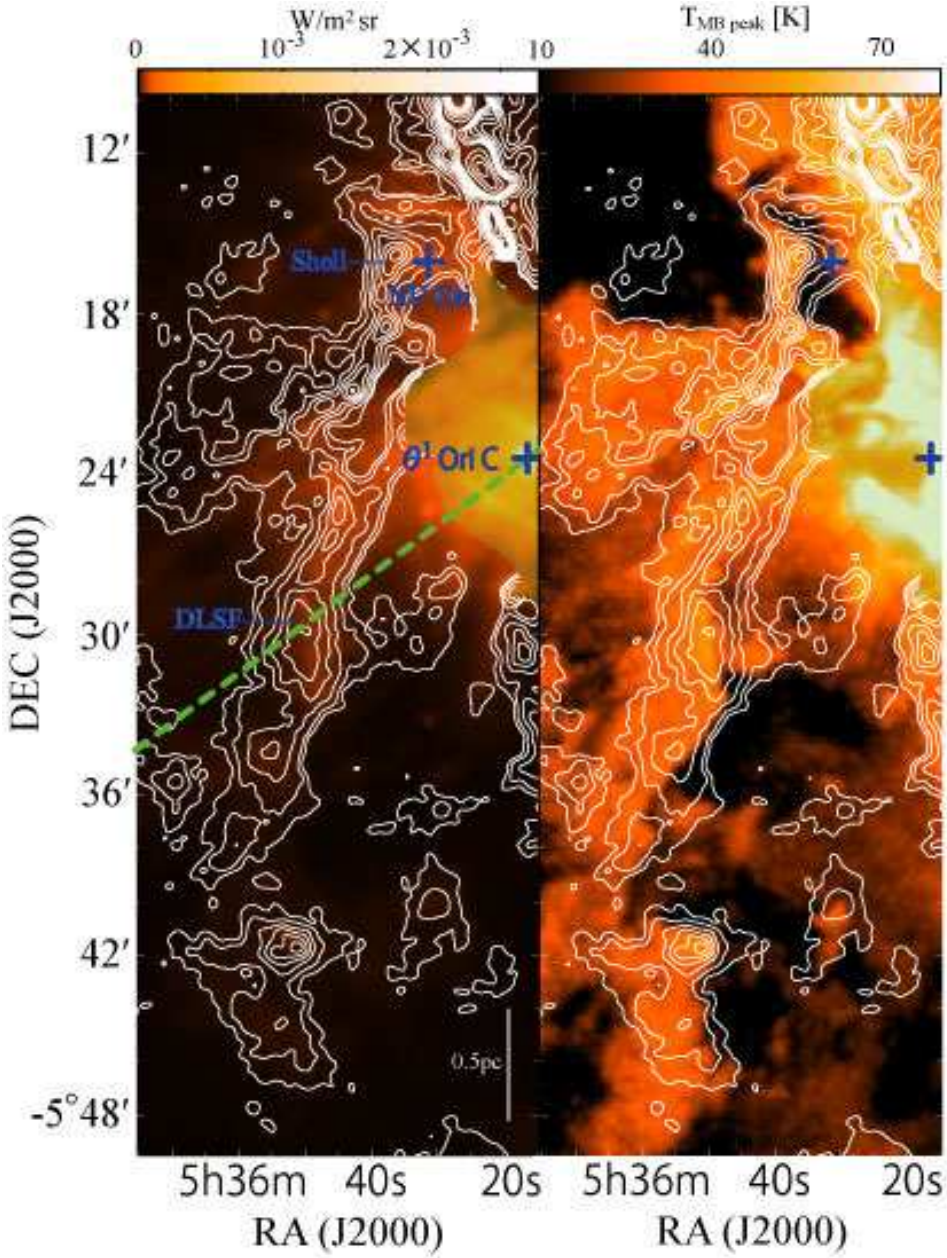

Fig. 9. (a) AzTEC 1.1 mm contours overlaid on a MSX 8 μm map in the M 43 and DLSF region. (b) AzTEC 1.1 mm contours overlaid on a peak intensity map in the ^{12}CO (J=1–0) line in the M 43 and DLSF region. Contour levels start from 5 σ with an interval of 10 σ for a range of 10 - 100 σ and 50 σ for a range from 100 σ. The crosses show the position of NU Ori and θ^1 Ori C, respectively. The green dash line shows a cut line of the intensity profiles shown in Figure 17.

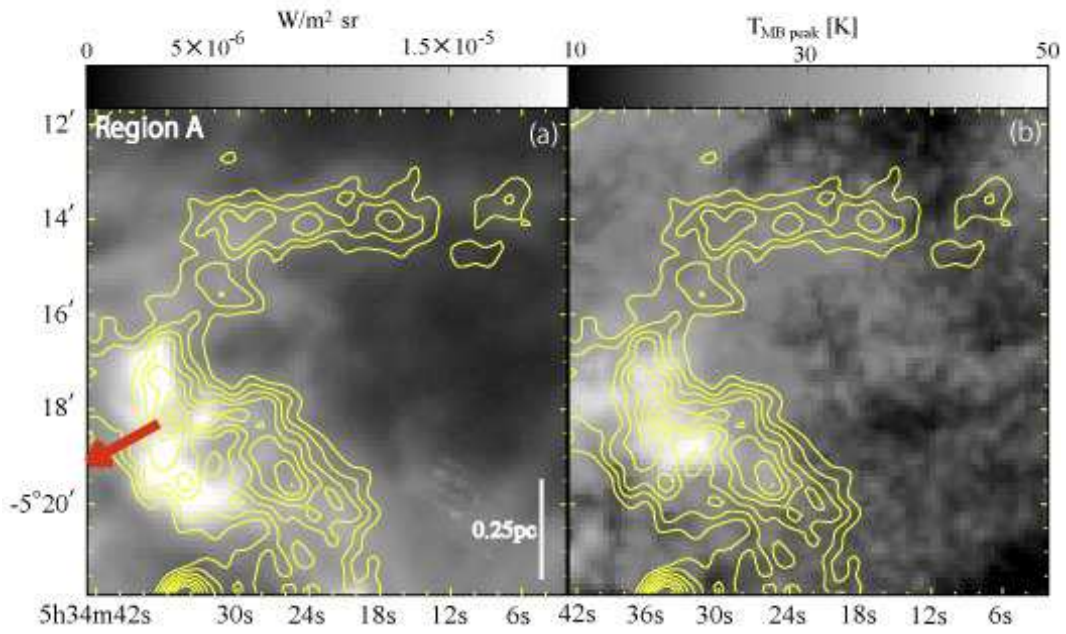

Fig. 10. AzTEC/ASTE 1.1 mm contours overlied on a MSX 8 μm map and peak intensity map in the ^{12}CO (J=1–0) line in Region A. Contour levels start from 10 σ with an interval of 10 σ for a range of 10 - 150 σ and 50 σ for a range from 150 σ.

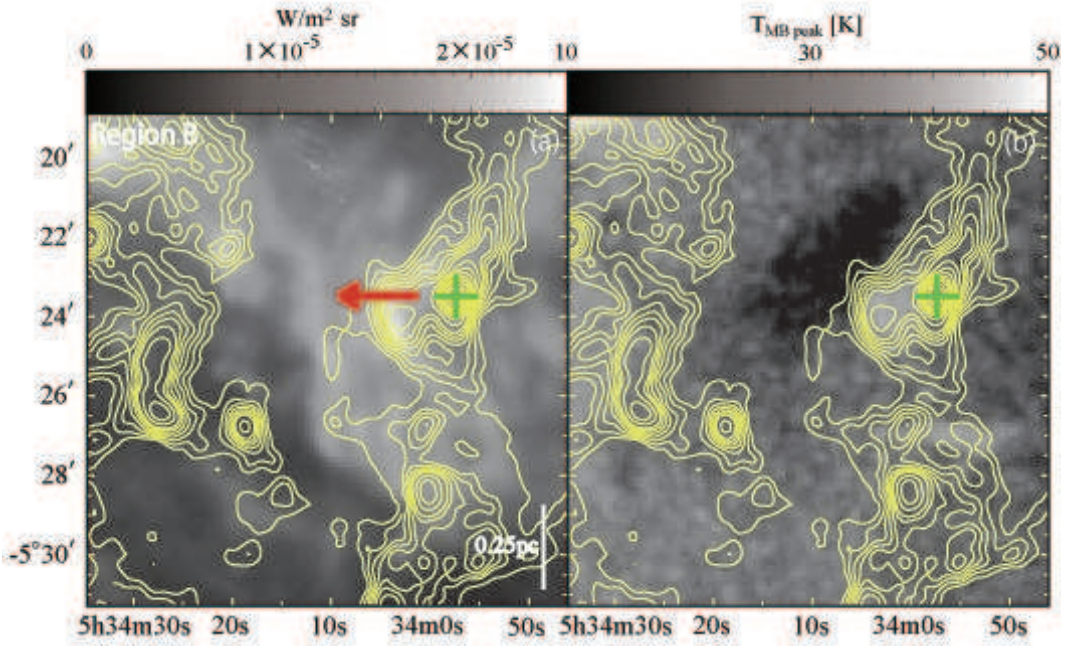

Fig. 11. AzTEC/ASTE 1.1 mm contours overlied on a MSX 8 μm map and peak intensity map in the ^{12}CO (J=1–0) line in Region B. Contour levels start from 10 σ with an interval of 10 σ for a range of 10 - 150 σ and 50 σ for a range from 150 σ.

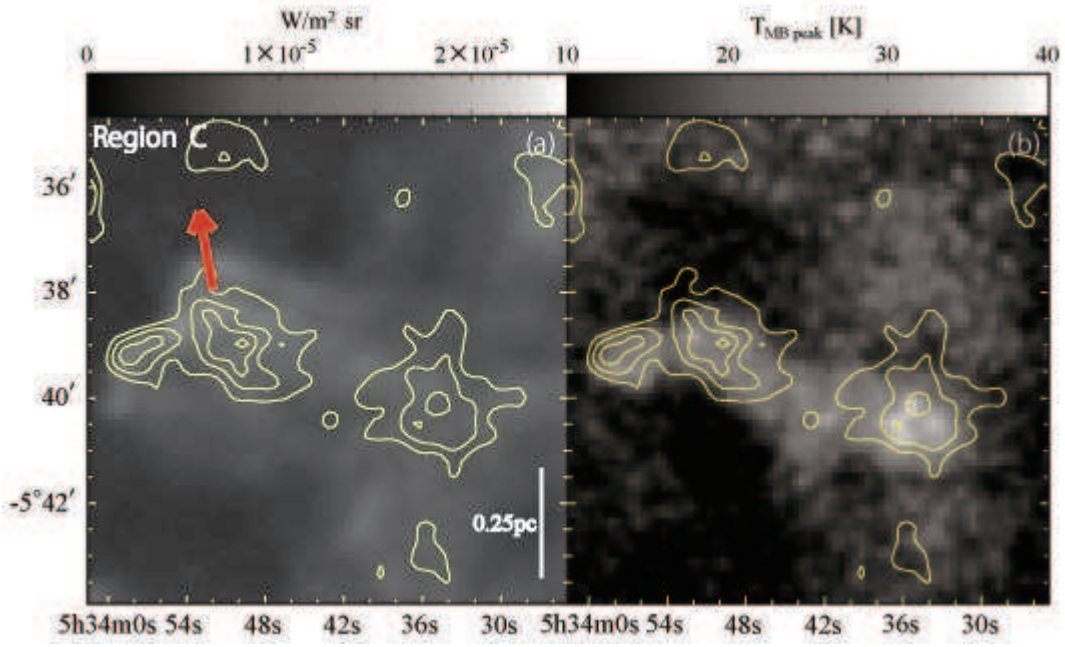

Fig. 12. AzTEC/ASTE 1.1 mm contours overlied on a MSX 8 μm map and peak intensity map in the ^{12}CO (J=1–0) line in Region C. Contour levels start from 10 σ with an interval of 10 σ for a range of 10 - 150 σ and 50 σ for a range from 150 σ.

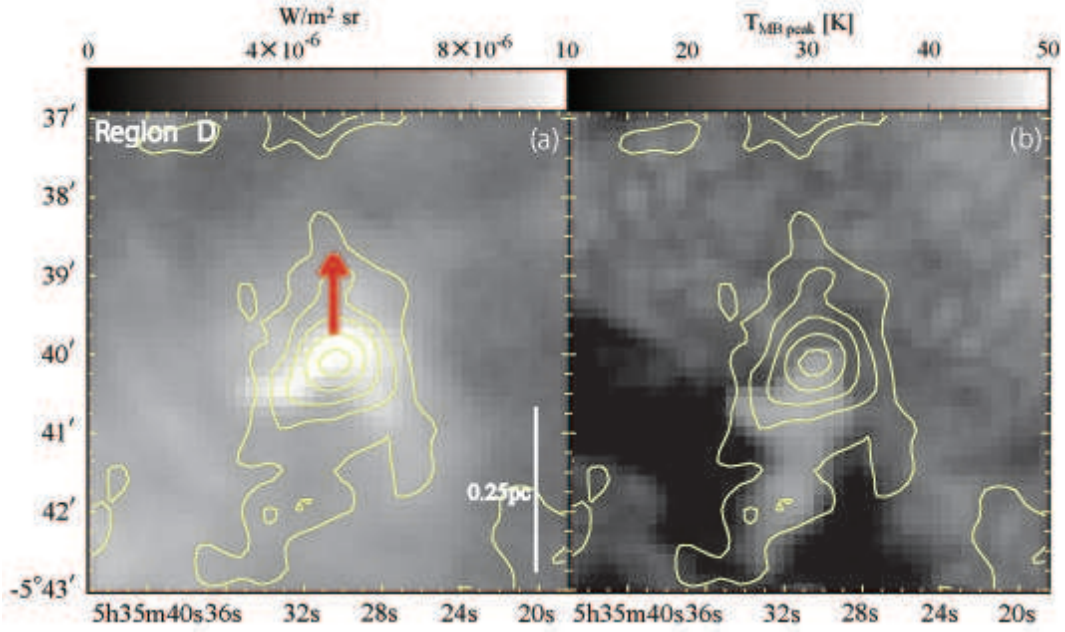

Fig. 13. AzTEC/ASTE 1.1 mm contours overlied on a MSX 8 μm map and peak intensity map in the ^{12}CO (J=1–0) line in Region D. Contour levels start from 10 σ with an interval of 10 σ for a range of 10 - 150 σ and 50 σ for a range from 150 σ.

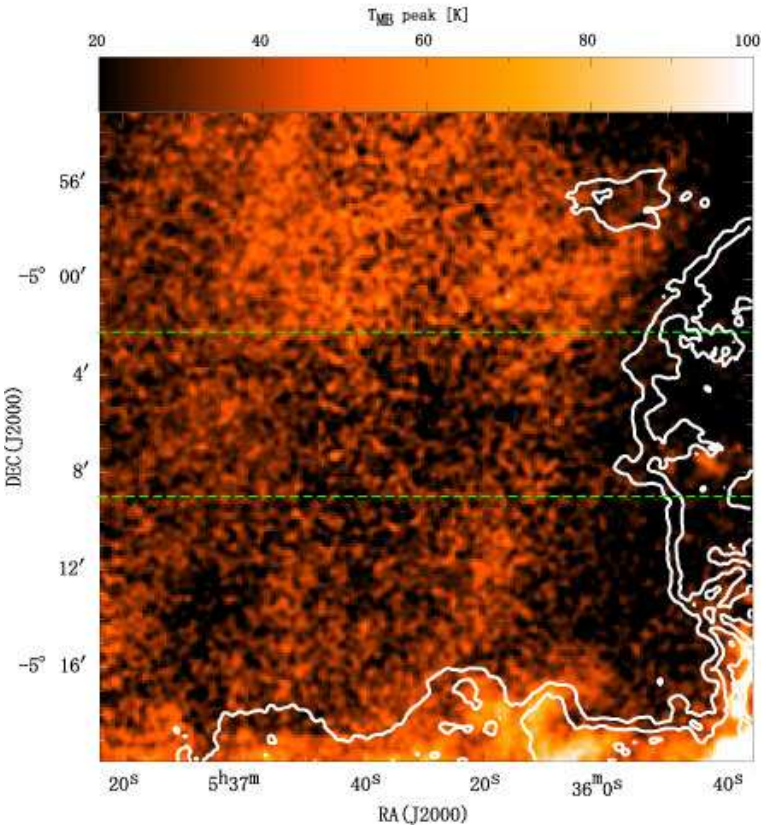

Fig. 14. ^{12}CO (J=1–0) peak intensity map (contour) superposed on the image of diffuse ^{12}CO (J=1–0) components (color) in the east of the OMC-2/3 region. A velocity range of the diffuse CO components is 2.6 - 8.6 km s^{-1}. The integrated velocity range of the image of diffuse CO components is 2.6 - 8.6 km s^{-1}. Contour levels are 15, 30, 45 K in $T_{\rm MB}$.

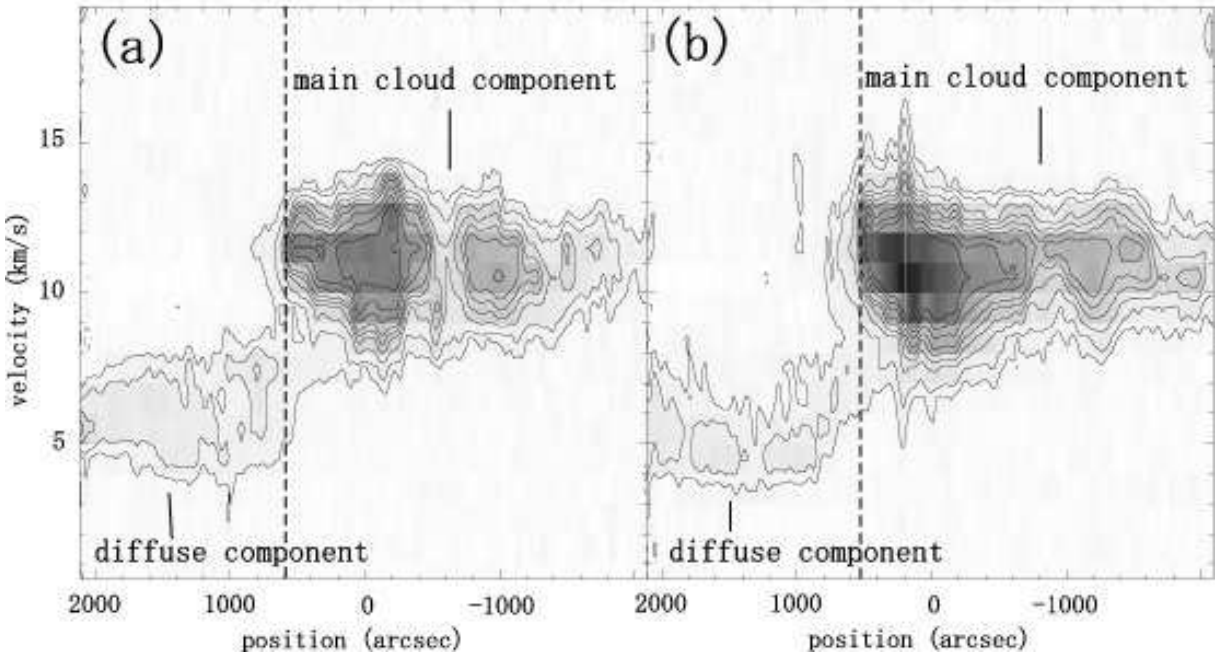

Fig. 15. Position-Velocity (P-V) diagrams of the ^{12}CO (J=1–0) emission. The cut lines are shown in Figure 14. The declination of the cut lines is $-5°2'26.''14$ and $-5°9'6.''03$, respectively. Vertical lines show the position of CO front. Contour levels start at 2 σ levels with an interval of 2 σ.

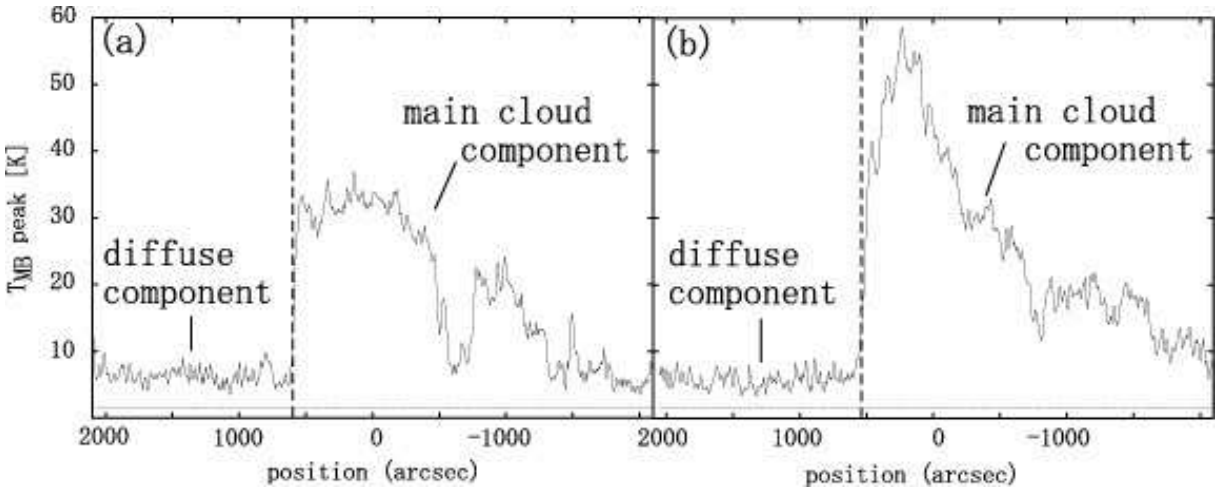

Fig. 16. Peak intensity profiles of the ^{12}CO (J=1–0) emission. The cut lines is shown in Figure 14. The declination of the cut lines are $-5°2'26.''14$ and $-5°9'6.''03$, respectively. Vertical dash lines show the position of CO front. Horizontal lines show the noise level (1 σ = 1.4 K at $T_{\rm MB}$) at the velocity channel maps with a velocity width of 0.4 km s^{-1}.

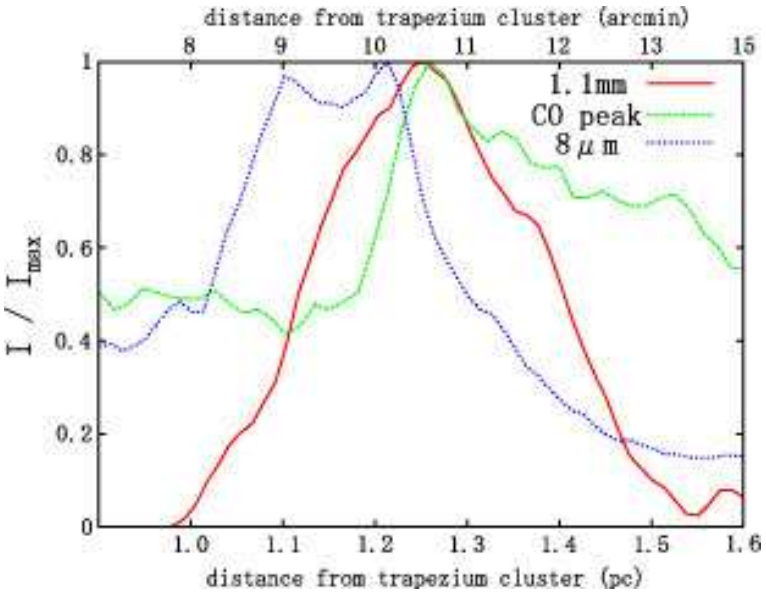

Fig. 17. Intensity profiles of the 1.1 mm continuum emission, ^{12}CO $T_{\rm MB}^{\rm peak}$ peak, and 8 μm emission, whose cut line is shown in Figure 9, as a function of the distance from trapezium cluster (θ^1 Ori C).

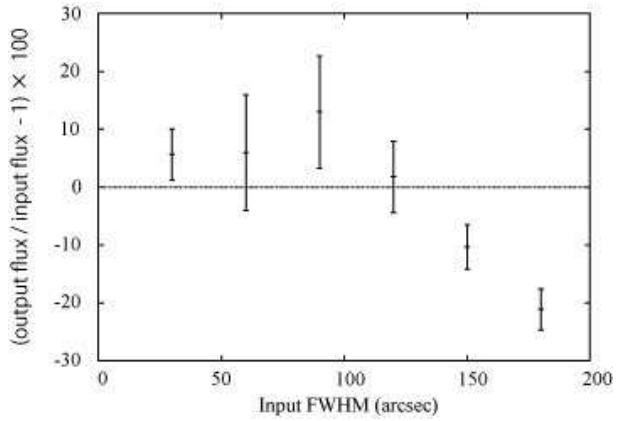

Fig. 18. Fraction of the over-estimated (positive) or missed (negative) flux as a function of the FWHM size of the input model Gaussian.

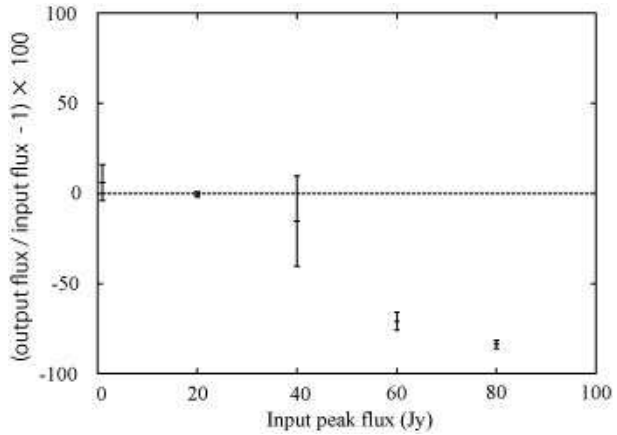

Fig. 19. Fraction of the over-estimated (positive) or missed (negative) flux as a function of the peak flux of the input model Gaussian.

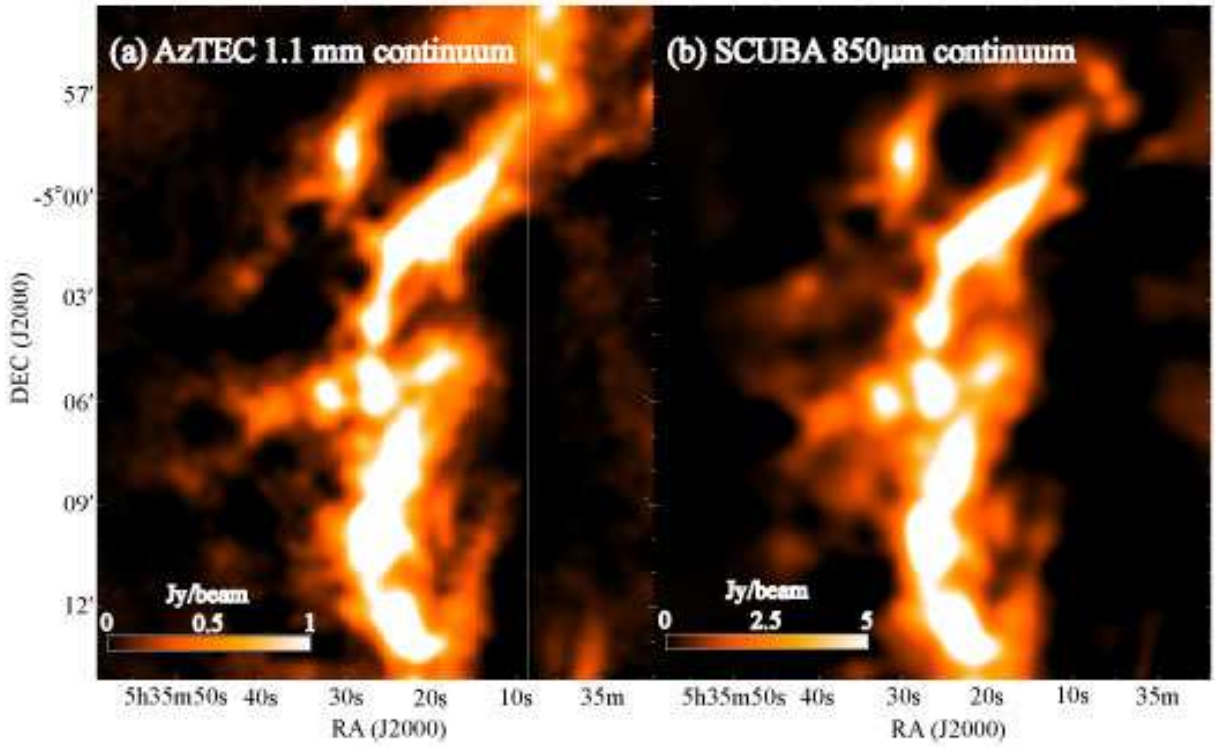

Fig. 20. (a) AzTEC FRUIT map in the OMC-2/3 region. (b) SCUBA 850 μm map in the OMC-2/3 region obtained by Johnstone & Bally (1999).

Table 1. PARAMETERS FOR OBSERVATIONS

Telecope/Receiver	ASTE / AzTEC	NRO 45 m / BEARS
Line / Wavelength	1.1 mm	^{12}CO (J=1–0;115.271 GHz)
Observation date	Oct. 2008 - Dec. 2008	Nov. 2007 - May 2008
Observing mode	raster	OTF
Observation time	15 hr	40 hr
Mapping size	$1.^{\circ}7 \times 2.^{\circ}3$	$1.^{\circ}2 \times 1.^{\circ}2$
Effective beam size	$40''$	$21''$
Velocity width	——	1.0 km s^{-1}
Typical r.m.s.	9 mJy beam^{-1}	0.9 K